

# Configuration and validation of an oceanic physical and biogeochemical model to investigate coastal eutrophication in the Southern California Bight

Fayçal Kessouri<sup>1,2</sup>, Karen McLaughlin<sup>1</sup>, Martha Sutula<sup>1</sup>, Daniele Bianchi<sup>2</sup>, Minna Ho<sup>1</sup>, James C McWilliams<sup>2</sup>, Lionel Renault<sup>2,3</sup>, Jeroen Molemaker<sup>2</sup>, Curtis Deutsch<sup>4</sup>, Anita Leinweber<sup>2</sup>

<sup>1</sup>Southern California Coastal Water Research Project, Costa Mesa, CA <sup>2</sup>Department of Atmospheric and Oceanic Sciences, University of California Los Angeles, CA <sup>3</sup>Laboratoire d'Études en Géophysique et Océanographie Spatiale, Toulouse, France <sup>4</sup>School of Oceanography, University of Washington, WA

## Key Points:

- The model reproduces gradients of physical and biogeochemical properties in the SCB, including seasonal, interannual, and ENSO variability.
- Resolving submesoscale currents increases the vertical flux of nutrients, and allows realistic reproduction of wastewater plume circulation.
- Wastewater and riverine inputs are consistent with intensified nutrients, productivity, export, and remineralization nearshore.

---

Corresponding author: F. Kessouri and K. McLaughlin, [faycalk@sccwrp.org](mailto:faycalk@sccwrp.org) ; [karenm@sccwrp.org](mailto:karenm@sccwrp.org)

This article has been accepted for publication and undergone full peer review but has not been through the copyediting, typesetting, pagination and proofreading process, which may lead to differences between this version and the [Version of Record](#). Please cite this article as [doi: 10.1029/2020MS002296](https://doi.org/10.1029/2020MS002296).

This article is protected by copyright. All rights reserved.

## Abstract

The Southern California Bight (SCB), an eastern boundary upwelling system, is impacted by global warming, acidification and oxygen loss, and receives anthropogenic nutrients from a coastal population of 20 million people. We describe the configuration, forcing, and validation of a realistic, submesoscale resolving ocean model as a tool to investigate coastal eutrophication. This modeling system represents an important achievement because it strikes a balance of capturing the forcing by U.S. Pacific Coast-wide phenomena, while representing the bathymetric features and submesoscale circulation that affect the transport of nutrients from natural and human sources. Moreover, the model allows simulations at timescales that approach the interannual frequencies of ocean variability. The model simulation is evaluated against a broad suite of observational data throughout the SCB, showing realistic depiction of the mean state and its variability with satellite and *in situ* measurements of state variables and biogeochemical rates. The simulation reproduces the main structure of the seasonal upwelling front, the mean current patterns, the dispersion of wastewater plumes, as well as their seasonal variability. Furthermore, it reproduces the mean distributions of key biogeochemical and ecosystem properties and their variability. Biogeochemical rates reproduced by the model, such as primary production and nitrification, are also consistent with measured rates. This validation exercise demonstrates the utility of using fine-scale resolution modeling and local observations to identify, investigate, and communicate uncertainty to stakeholders to support management decisions on local anthropogenic nutrient discharges to coastal zones.

## Plain Language Summary

We applied and validated an ocean numerical model to investigate the effects of land-based and atmospheric nutrient loading on coastal eutrophication and its effects on carbon, nitrogen and oxygen cycles of the Southern California Bight, an upwelling-dominated marine embayment on the U.S. West Coast. The model is capable of high resolution, multi-year hindcast simulations, which enable investigations to disentangle natural variability, climate change, and local human pressures that accelerate land-based and atmospheric nutrient loads. The model performance assessment illustrates that it faithfully reproduces monitored ocean properties related to algal blooms, oxygen and water acidity, among others, that can be traced to land-based and atmospheric inputs of nutrients and carbon from human activities. The model performance assessment helps to constrain uncertainties in predictions to support ongoing conversations on approaches to reduce the effects of climate change, including considerations of management of local nutrient and carbon inputs.

## 1 Introduction

Human-driven eutrophication has resulted in profound impacts to coastal ecosystems around the world. These impacts are arguably the best studied in estuaries and enclosed bays (e.g. Chesapeake Bay; Cerco and Cole (1993); Boesch et al. (2001)) and semi-enclosed seas such as the Baltic Sea (Savchuk & Wulff, 2007; Cederwall & Elmgren, 1990), the Mediterranean Sea (Arhonditsis et al., 2000), and the Gulf of Mexico (Justić et al., 2005; Laurent et al., 2018). To date, few investigations of coastal eutrophication have occurred in Eastern Boundary Upwelling systems (EBUS). While strong upwelling and vigorous surface currents would generally limit the extent to which coastal eutrophication could occur (Fennel & Testa, 2019), such investigations have also been limited by coupled physical biogeochemical numerical modeling approaches that can adequately resolve fine-resolution bathymetry and the complexities of submesoscale circulation (McWilliams, 2016; Dauhajre et al., 2019), while simulating a sufficient duration (several years) to distinguish oceanic versus terrestrial forcing. These submesoscale circulation features, including fine scale eddies and filaments < 5 km in horizontal resolution, strongly control the magnitude and variability of nearshore upwelling and associated nutrient transport. Thus, high resolution, submesoscale-resolving

68 numerical models are a necessary prerequisite for mechanistic modeling studies and source  
69 attribution of oceanic versus terrestrial drivers of coastal eutrophication in EBUS. Inad-  
70 adequate modeling system and lack of numerical model validation have been identified as  
71 significant barriers to effective, evidence-based solutions to coastal eutrophication (Boesch,  
72 2019).

73 All the necessary ingredients are present to motivate a numerical modeling investigation  
74 of the role of coastal eutrophication in driving ocean acidification and oxygen loss in the  
75 Southern California Bight (SCB), a large marine open embayment found in the California  
76 Current System (CCS) on the U.S. Pacific Coast. First, the SCB is a biologically-productive  
77 region, and thus of high economic and ecological importance. Seasonal upwelling of nutrient-  
78 rich deep water maintains high rates of biological productivity over broad scales. At the  
79 same time, upwelling draws water masses that are naturally low in dissolved oxygen, pH,  
80 and carbonate saturation state ( $\Omega_{Ar}$ ) onto the shelf and into the photic zone (Sutton et al.,  
81 2017). Second, the SCB has one of the most spatially comprehensive and longest-running  
82 coastal observational systems in the world. Several physical and biogeochemical variables  
83 are sampled regularly and extensively, creating an ideal setting for model-data comparisons.  
84 Third, the SCB is home to one of the most densely populated coastal regions in North Amer-  
85 ica, where the discharges of primary or secondary treated wastewater from a population of  
86 20 million people are released to the coastal zone via ocean outfalls, along with the urban  
87 and agricultural runoff from 75 rivers. These nutrient sources rival natural upwelling in  
88 magnitude (Howard et al., 2014), roughly doubling available nitrogen to nearshore coastal  
89 waters. Intensifying ocean acidification, oxygen loss and harmful algal blooms have moti-  
90 vated California policy makers to consider reducing anthropogenic nutrients as a climate  
91 change mitigation strategy (Ocean Protection Council, 2018), but wastewater treatment  
92 plant upgrades and methods to increase control or reduce non-point sources would cost  
93 billions. A numerical modeling approach is needed to disentangle the effects of natural  
94 upwelling and climate change from anthropogenic nutrient loading from land-based and  
95 atmospheric sources.

96 To support such investigations, the regional oceanic model system (ROMS, Shchepetkin  
97 and McWilliams (2005)) coupled to the biogeochemical elemental cycling model (BEC,  
98 Moore et al. (2004)) has been recently adapted for the CCS (Renault et al., 2021; Deutsch  
99 et al., 2021). A downscaled model domain was established, scaling from a 4 km horizon-  
100 tal resolution configuration spanning the entire CCS, to a 1 km resolution grid covering  
101 the much of the California coast (latitude  $< 40.25^\circ\text{N}$ ), to a 0.3 km grid in the Southern  
102 California Bight (SCB), where investigations of local anthropogenic inputs were focused.  
103 Modeling experiments investigating submesoscale transport (captured at model resolutions  
104  $\leq 1$  km) have demonstrated an up to ten-fold increase in the magnitude of instantaneous  
105 vertical N fluxes (Kessouri, Bianchi, et al., 2020) relative to mesoscale transport represented  
106 by a 4 km model (Section 2.2). Furthermore, a finer horizontal resolution of bathymetry  
107 improves the representation of coastal currents, submesoscale circulation, and coast-offshore  
108 connectivity (Dauhajre et al., 2019). For this reason, investigations of coastal eutrophica-  
109 tion are simulated here at 0.3 km horizontal resolution. Simulations conducted with the 4  
110 km ROMS-BEC model domain have been validated for regional-scale atmospheric forcing,  
111 physics, and biogeochemistry, including  $\text{O}_2$ , carbonate saturation state, primary productiv-  
112 ity, and hydrographic parameters, demonstrating that the model captures broad patterns  
113 of critical properties in the CCS (Renault et al., 2021; Deutsch et al., 2021). However, ad-  
114 ditional focused validation of nearshore, anthropogenically-enhanced gradients in nutrients,  
115 primary production, oxygen and pH in model simulations conducted at 0.3 km resolution  
116 are needed to gauge model utility to investigate the impacts of coastal eutrophication on  
117 ocean acidification and oxygen loss.

118 We employed this downscaled, submesoscale-resolving physical-biogeochemical model  
119 to investigate the effects of land-based and atmospheric nutrient inputs in driving coastal  
120 eutrophication and ocean acidification and oxygen loss (Kessouri et al., 2021). The aim of

121 this manuscript is to: 1) document the SCB ROMS-BEC model configuration, including the  
122 effects of land-based and atmospheric inputs of nutrients and organic carbon, intended to  
123 support investigations of coastal eutrophication, and 2) present a validation of SCB ROMS-  
124 BEC simulations against available observations, focusing on anthropogenically-enhanced  
125 gradients in nutrients, primary production, oxygen, and pH.

## 126 **2 SCB coupled physical and biogeochemical model description, configura-** 127 **tion and forcing**

### 128 **2.1 Model description**

#### 129 *2.1.1 Ocean hydrodynamics*

130 Ocean hydrodynamics is modeled with the Regional Oceanic Modeling System (ROMS)  
131 (Shchepetkin & McWilliams, 2005), a free-surface, terrain-following coordinate model with  
132 3-D curvilinear coordinates that solves the primitive equations with split-explicit time steps.  
133 It contains state-of-art numerical algorithms that provide an accurate and stable representa-  
134 tion of physical processes down to scales of tens of meters, and allows for offline downscaling  
135 of high-resolution sub-domains within larger domains. The offline downscaling is based  
136 on the Orlanski scheme for the baroclinic mode (Marchesiello et al., 2001) and a modified  
137 Flather scheme for the barotropic mode (Mason et al., 2010). Vertical mixing in the bound-  
138 ary layers is represented by a K-profile parameterization (W. G. Large et al., 1994). The  
139 U.S. West Coast hindcast model has been successfully run over two decades (between 1997  
140 and 2017) at 1 and 4 km horizontal resolution using high-resolution spatial and temporal  
141 atmospheric forcing that represent the effects of wind drop-off, the current feedback on the  
142 surface stress, and high-frequency wind fluctuations (Renault, Hall, & McWilliams, 2016a;  
143 Renault, Molemaker, McWilliams, et al., 2016). For this study, we further downscale to  
144 0.3-km resolution to capture submesoscale processes.

#### 145 *2.1.2 Biogeochemistry*

146 Ocean biogeochemical modeling approaches can have a broad range of complexities,  
147 ranging from few functional groups (e.g. NPZD models, Fasham (1993)), to multiple biogeo-  
148 chemical cycles (e.g. C, N, O) and plankton functional groups. To provide a representation  
149 of biogeochemical cycles, ROMS is dynamically coupled to the Biogeochemical Elemental  
150 Cycling (BEC) model (Moore et al., 2004; Gruber, 2004; Gruber et al., 2011; Deutsch et  
151 al., 2021). A schematic of BEC is shown in Fig. 1(b). BEC is a multi-element (C, N, P,  
152 O, Fe, Si) and multiplankton model that includes three explicit phytoplankton functional  
153 groups (picoplankton, silicifying diatoms, N-fixing diazotrophs), one zooplankton group,  
154 and dissolved and sinking organic detritus. The impacts of calcifying phytoplankton (coc-  
155 colithophores) on the carbon system is represented implicitly. Remineralization of sinking  
156 organic material follows the multi-phase mineral ballast parameterization of Armstrong et  
157 al. (2001). Sedimentary processes have also been expanded. Particulate organic  
158 matter reaching the sediment is accumulated and slowly remineralized with a timescale of  
159 330 days, to provide a buffer between particle deposition and nutrient release. Nitrogen loss  
160 to the sediment is parameterized according to the empirical diagenetic model for sediment  
161 denitrification of Middelburg et al. (1996). Water column denitrification is only active when  
162 oxygen concentrations fall below  $5 \text{ mmol m}^{-3}$ . Sedimentary release of Fe is based on the  
163 benthic chamber measurements of (Severmann et al., 2010) for the California-Oregon coast,  
164 and increases as bottom water oxygen concentrations decrease. Atmospheric dust deposition  
165 follows the parameterization by Mahowald et al. (2006) and provides an additional source  
166 of iron at the surface, although of minor importance compared to sedimentary iron release  
167 in the region (Deutsch et al., 2021). The ecosystem is linked to a carbon system module  
168 that tracks dissolved inorganic carbon (DIC) and alkalinity, and an air-sea gas exchange  
169 module that allows realistic representation of dissolved gases (e.g.  $\text{O}_2$ ,  $\text{CO}_2$  and nitrous  
170 oxide), based on the formulation of Wanninkhof (1992).

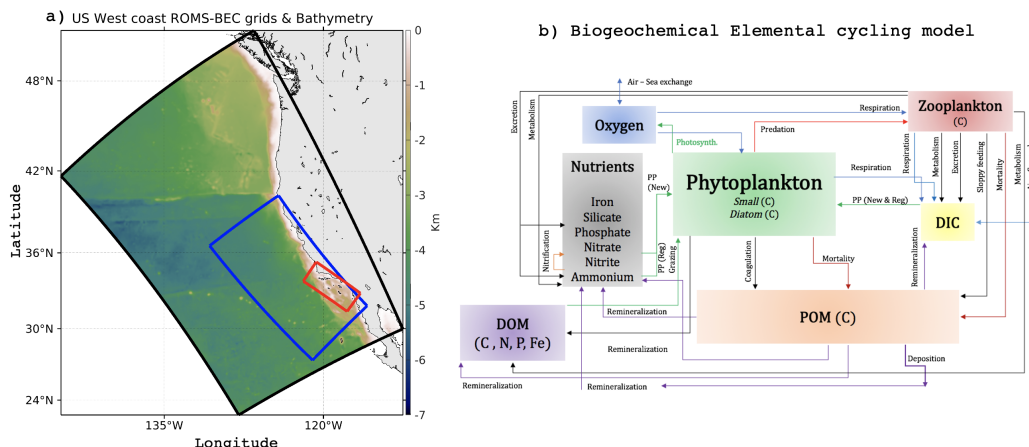


Figure 1: a) ROMS-BEC model configurations.  $dx = 4$  km is the black box,  $dx = 1$  km is the blue box,  $dx = 0.3$  km is the red box. Background color shading show the topography from  $dx = 4$  km. b) Schematic of the biogeochemical elemental cycling model. The schematic shows state variables (boxes) and biogeochemical rates and feedback (arrows).

### 2.1.3 SCB Model configuration

The SCB model domain extends along a 450 km stretch of the coast, from Tijuana to Pismo Beach, and about 200 km offshore. This grid, shown in Fig. 1a), is composed of 1400 x 600 grid-points, with a nominal resolution of  $dx = 0.3$  km. The grid has 60  $\sigma$ -coordinate vertical levels using the stretching function described in Shchepetkin and McWilliams (2009), with the following stretching parameters:  $\theta_s = 6$ ,  $\theta_b = 3$ , and  $h_c = 250$ -m. The model is run with a time step of 30 seconds, and outputs are saved as 1-day averages.

The oceanic forcing of the 0.3 km domain originates from multi-level offline downscaling. A 4-km simulation is initialized and forced at the open boundaries by a preexisting North-east Pacific-wide ROMS solution at 12-km resolution (Renault et al., 2021), initialized and forced on the boundaries by the global model Mercator Glorys2V3 (<http://www.myocean.eu>) for the physics, and with reconstruction of biogeochemical fields using world ocean database. We used climatological fields for organic material, and relationships with density for nutrients. Full description of the boundary conditions and initialization of the parent configuration at 12-km can be found in Deutsch et al., 2021. The 4-km configuration is run for the period 1995-2017, after a spin-up of 2 years. A 1 km simulation is initialized and forced from the 4-km model, including initial conditions and open boundary conditions, starting in October 1996 and ending in December 2007. The 0.3-km simulation is initialized and forced at its boundaries by the 1-km simulation starting from January 1997 and ending in December 2000. The bathymetry used in this configuration comes from the Southern California Coastal Oceanic Observation System (SCCOOS) 3 Arc-Second Coastal Relief Model Development (90-m horizontal resolution).

The oceanic model is forced by hourly outputs from the atmospheric uncoupled Weather Research and Forecast model (WRF06; Skamarock and Klemp (2008)). Using bulk formulae (W. B. Large, 2006), WRF06 provides heat, surface evaporation, momentum and atmospheric data and is run at 6 km resolution over a domain similar to the 4-km (Fig. 1 and used for Renault, Hall, and McWilliams (2016b)), and includes a wind-current coupling parameterization necessary to attain more realistic simulations of the oceanic eddy kinetic energy (EKE) and circulation (Renault, Molemaker, McWilliams, et al., 2016; Renault et al., 2020).



Model simulations were conducted from 1997-2000, a period chosen to capture the effects of all three phases of the El Niño–Southern Oscillation (ENSO); it also captures the beginning of the "modern" state of point source management in the SCB, where several large Publicly Owned Treatment Plants (POTW) were in transition from primary to secondary treatment. (We will refer to submarine point sources outfalls from the treatment plants as "POTW" hereafter.)

## 2.2 Importance of submesoscale circulation

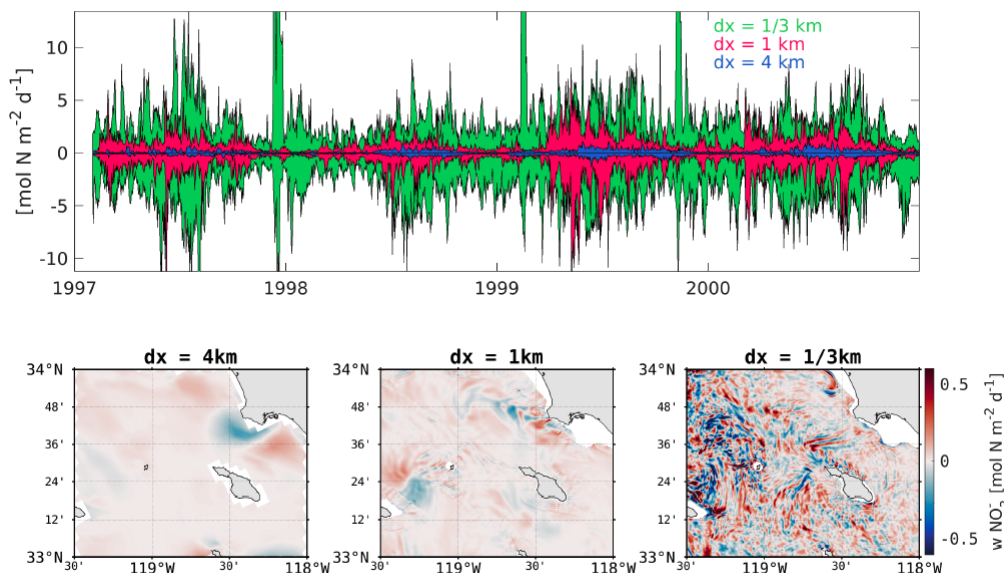


Figure 2: (Upper panel) Timeseries (1997-2001) of the vertical eddy flux of nitrate at 40-m depth calculated as follow:  $\overline{wN} = \overline{wN} + \overline{wN'}$ , where the overbar represents a monthly average, and the prime the deviation from this average, for region covering the entire Southern California Bight (31.4-35.3N and 116.5-121.8W). The minimum and maximum values (i.e. the envelope) of the flux are shown in blue for the 4-km solution, in red for the 1-km solution and in green for the 1/3 km. (Lower panel) Snapshot of the vertical flux of nitrate in spring at 40-m off the coast of Palos Verdes that shows higher magnitudes and enhanced variability as resolution increases.

Downscaling to  $dx = 0.3$ -km allows the model to represent ocean circulation that includes baroclinic and barotropic eddies and turbulence generated at the submesoscale (Capet, Campos, & Paiva, 2008). Submesoscale dynamics energizes frontogenesis by mesoscale straining and mixed layer instabilities (Capet, Klein, et al., 2008; Capet, Campos, & Paiva, 2008; Capet, McWilliams, et al., 2008). Oceanic fronts are a driver of significant nutrient supply to the upper ocean. They have also been recognised as areas of enhanced biomass in many regions of the global ocean (Woodson & Litvin, 2015), as well as important locations for fisheries (e.g. (Galarza et al., 2009)). Resolving submesoscale eddies dramatically increases the variability of vertical fluxes of biogeochemical tracers and other material properties, eventually allowing a more accurate representation of chemical and biological constituents. Fig. 2 (upper panel) shows the temporal variability and horizontal distribution of vertical eddy fluxes of nitrate at 40-m from 3 different resolutions with the ROMS-BEC model (see section 2.1.3). Submesoscale dynamics increase instantaneous fluxes by more than one order of magnitude, with more frequent and vigorous fine-scale structures (Fig. 2,

222 bottom panels) when increasing the resolution from 4-km to 1-km, and similarly another  
223 order of magnitude when increasing resolution from 1 km to 0.3-km. Intensification of ver-  
224 tical flux of nitrate at the euphotic depth has previously been shown in idealized models  
225 (Mahadevan, 2016; Lévy et al., 2012) and in realistic simulations in the central California  
226 upwelling system (Kessouri, Bianchi, et al., 2020), but has never been modeled in the SCB  
227 at this resolution. The impact of the submesoscale on nutrients fluxes is more apparent  
228 during winter, when the mixed layer is deeper, wind forcing more intense, and submesoscale  
229 circulation more energetic. During this period, nutrients are transported from the nutri-  
230 cline by transient fronts that can last only few days, and are only properly resolved in the  
231 0.3km configuration. Submesoscale eddies have been associated with increased productivity  
232 in the oligotrophic ocean (Mahadevan, 2016) and decreased productivity in the upwelling  
233 region (Kessouri, Bianchi, et al., 2020). Our submesoscale-resolving simulation at  $dx =$   
234 0.3-km is an opportunity to quantify the balances of nitrogen, dissolved oxygen, carbon and  
235 productivity using a more realistic representation of the physical circulation, as well as a  
236 representation of urban anthropogenic inputs to the ocean.

237 Our simulations show that the increased number of fronts and submesoscale instabili-  
238 ties promote intense variability of nitrate transport, as shown in Fig. 2, as well as increased  
239 heterogeneity at the subsurface chlorophyll *a* maximum. However, surface phytoplankton  
240 biomass is only intensified if the timescale of the enrichment is sufficiently long and main-  
241 tained in these small scale features. We argue that modeling at this scale allows for a more  
242 accurate simulation of biogeochemical tracers and rates, as described in subsequent sections.  
243 However, we also note that comparing the model and observations to highlight the realism of  
244 submesoscale processes is challenging, mostly because of the lack of observations of biogeo-  
245 chemical variables at high enough spatial and temporal resolution. Furthermore, changes  
246 in the distribution of biogeochemical tracers as the model resolution increases are relatively  
247 subtle (Kessouri, Bianchi, et al., 2020), and in general within the range of variability of  
248 observations and simulations. By construction, the submesoscale-resolving model better  
249 represents scales relevant to coastal circulation and anthropogenic nutrient emission and  
250 dispersal, and the underlying dynamics (Capet, Campos, & Paiva, 2008). Showing that this  
251 configuration indeed compares realistically with observations, in an average and statistical  
252 sense, strongly supports the validity of the model for coastal biogeochemical applications,  
253 even though aspects of the simulations such as submesoscale processes remain challenging  
254 to directly assess.

### 255 **2.3 Terrestrial and atmospheric forcing of freshwater, nutrients and carbon**

256 Model simulations were forced with a monthly time series of spatially-explicit inputs  
257 (Fig. 3, upper), including freshwater flow, nitrogen, phosphorus, silica, iron, and organic  
258 carbon representing natural and anthropogenic sources (Sutula et al., 2021b). These data  
259 include POTW ocean outfalls and riverine discharges (1997-2017) and spatially-explicit  
260 modeled estimates of atmospheric deposition. POTW effluent data were compiled from per-  
261 mit monitoring databases and communication with sanitary agencies. Monthly time series  
262 of surface water runoff from 75 rivers are derived from model simulations and monitoring  
263 data (Sutula et al., 2021b). Direct atmospheric deposition is derived from the Community  
264 Multi-scale Air Quality (CMAQ) model (Byun et al., 2006), and follows the implementation  
265 of Deutsch et al. (2021). In this paper, we discuss in detail the formulation of the river and  
266 wastewater outfall inputs.

### 267 **2.4 Configuration of river and wastewater outfall forcing in the model**

Ocean outfalls and coastal rivers are modeled as mass sources into the ocean (Fig. 3,  
upper). To accomplish this, we add explicit volume fluxes to the otherwise divergence-free  
flow in the ocean. The inclusion of these fluxes makes it possible to account for associated  
sources of tracers, while satisfying conservation laws. Specifically, our approach allows for  
the proper influx of fresh water in the ocean, without resorting to a ‘virtual salt’ flux,

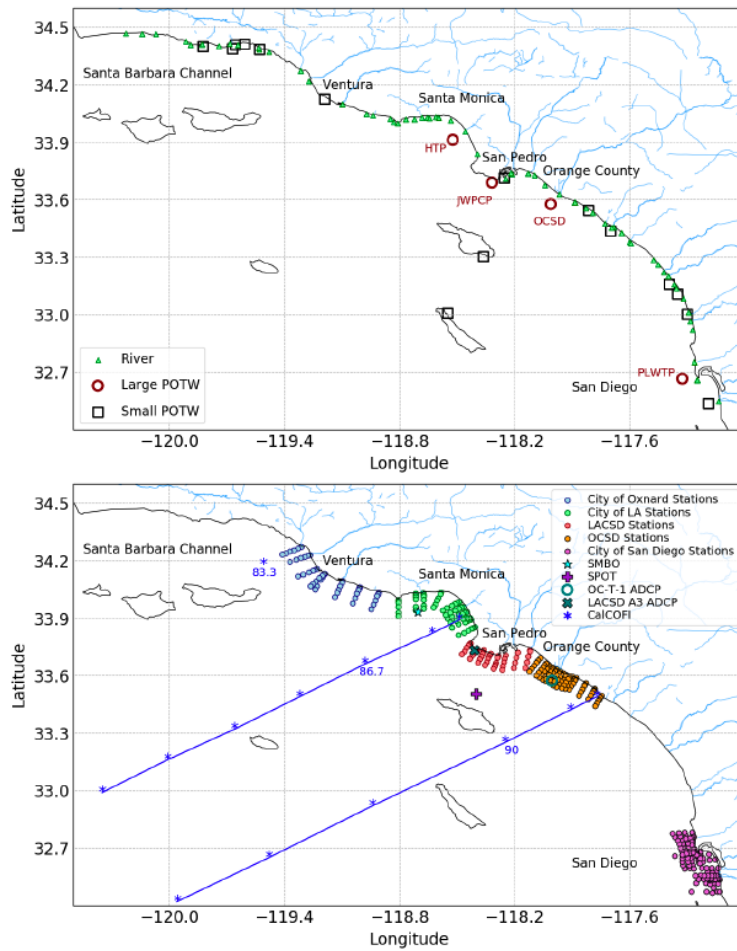


Figure 3: (Upper panel) Location of rivers and POTW outfalls along the SCB. (Lower panel) Location of monitoring stations used for the validation, including POTW quarterly monitoring surveys, CalCOFI seasonal observations, showing the line numbers, Santa Monica Bay Observatory (SMBO), and San Pedro Oceanographic Timeseries (SPOT), mooring.



which is a common approach in larger scale ocean models (Kang et al., 2017). Since we explicitly include known volume fluxes for both rivers and outfall pipes, specification of tracer concentration is sufficient to correctly model the source terms. The tracer evolution equations that are used in ROMS are implemented by using control volumes (Shchepetkin & McWilliams, 2005) where for each tracer concentration  $C = C(x, y, z, t)$ ,

$$\frac{\partial \iiint C dV}{\partial t} = \iint u_n C dA. \quad (1)$$

where  $V = V(x, y, z, t)$  is the volume of the entire domain,  $u_n$  is the normal velocity into the volume and  $A = A(x, y)$  is the total area of grid cells source is being input. Additionally, we enforce mass conservation which implies;

$$\frac{\partial V}{\partial t} = \iint u_n dA. \quad (2)$$

In absence of rivers and outfalls, the flow is volume conservative, and the integral on the right hand side of Equation 2 is zero. Using Equations 1 and 2, it is easy to see that the mean concentration of a tracer can be lowered if the average concentration of the flux entering the control volume is less than the mean concentration in that volume. In this manner, fresh water rivers will lower the salinity of the water in which they enter. All 75 rivers and 23 POTW pipes that are considered in this study are implemented in this manner.

Each individual source is based on the following equation:

$$S(x, y, z, t) = \frac{W(x, y, z) Q_s(t) C_s(t)}{V_s} \quad (3)$$

With:

$S(x, y, z, t)$ : volume source of contaminant ( $\text{mmol m}^{-3} \text{ s}^{-1}$ ).

$W(x, y, z)$ : non-dimensional shape function (with values between 0 and 1).

$Q_s(t)$ : water volume flux from the source ( $\text{m}^3 \text{ s}^{-1}$ ).

$C_s(t)$ : concentration of the tracer C in the source water ( $\text{mmol m}^{-3}$ ).

$V_s$ : effective volume of the source ( $\text{m}^3$ ).

For each source,  $Q_s(t)$  and  $C_s(t)$  are prescribed as time series. The shape function  $W(x, y, z)$  distributes the tracer spatially and in the water column, representing non-resolved mixing and dilution effects. Its values represent the relative intensity of the *in situ* tracer injection, with values between 0 and 1. Tracer concentration C is distributed in the water column as  $C(x, y, z, t) = W(x, y, z)C_s(t)$  The effective 3D volume of the source is calculated from the shape function  $W(x, y, z)$  as:

$$V_s = \iiint W(x, y, z) dV \quad (4)$$

where the integral is over the model domain. For convenience, we assume that  $W(x, y, z)$  can be separated into a horizontal shape function  $A(x, y)$ , multiplied by a vertical shape function  $H(z)$  (both non-dimensional and with values between 0 and 1), such that:

$$V_s = \iint A(x, y) dx dy \int H(z) dz = A_s H_s \quad (5)$$

Here,  $A_s$  represents the effective source surface area ( $\text{m}^2$ ), and  $H_s$  the effective source thickness (m). The functions  $A(x, y)$  and  $H(z)$  are defined differently for POTW and rivers. They are assumed to be fixed in time; a time-dependent generalization (for example to mimic variations in the depth of the POTW buoyant plume) is straightforward. For POTW inputs, at each main diffuser, the horizontal distribution  $A(x, y)$  of the source is shown in Fig. S1. This method of weighting the plume in different cells allows the effluent to be

287 properly diluted vertically and horizontally at this resolution and prevents the model from  
 288 developing numerical instabilities.

Each large treatment plant has specialized outfall configurations that are taken into account for representation in the model (Fig. S1). The flow is divided in two at Hyperion Treatment Plant (HTP) located 6km off Marina Del Rey (Santa Monica Bay) (Fig. S1A) and Point Loma Wastewater Treatment Plant (PLWTP) in San Diego coast (Fig. S1D) to account for their Y-shaped diffuser, partitioning 50% of the flow to each diffuser. Orange County Sanitation District (OCSD) located 6km off Huntington Beach (Fig. S1C) has one flow through its L-shaped diffuser. Joint Water Pollution Control Plant (JWPCP) in Palos Verdes shelf (Los Angeles) (Fig. S1B) has three diffusers, the Y-shape northern typically discharges 17.5% of the flow for each leg of the Y-diffuser, and the southern L-shape diffuser discharges 65% of the flow. The vertical profile of the POTW sources is defined by a Gaussian function centered at a height  $z$  above the bottom ( $h_b$ ), to mimic a buoyant plume, so that  $H(z)$  is given by:

$$H(z) = e^{-z^2/d_s^2} \quad (6)$$

289 Where  $z = -h_b + h_s$ , with

290  $h_b$ : bottom depth (m).

291  $h_s$ : depth of the buoyant plume above the bottom (m).

292  $d_s$ : vertical scale of the POTW plume (m).

293 We further assume  $h_s = 20$  m and  $d_s = 10$  m, as in Uchiyama et al. (2014).

294 We distribute the SCB rivers on one horizontal grid point (0.3 km wide), where we  
 295 assume  $A(x, y) = 1$ , and similarly distribute the source vertically, with the Gaussian function  
 296 centered at the surface.  $h_s$  here is simply the water column depth to put the maximum input  
 297 at the surface. Because in ROMS the thickness of vertical grid cells varies in time, to ensure  
 298 tracer conservation the calculation of the input source volume  $V_s$  must be done at each time  
 299 step, even in the case of a time-independent source shape function  $W(x, y, z)$ . Effectively,  
 300 only  $H_s = H(z)$  needs to be recalculated at each time step.

### 301 3 Model performance assessment approach

302 The conceptual approach for model performance assessment is comprised of three com-  
 303 ponents, addressing different aspects of skill assessment: 1) statistical comparison of model  
 304 output to observational data for state variables by region and season; 2) comparison of model  
 305 output to observational data for biogeochemical rates; 3) evaluation of model behavior com-  
 306 pared to expected biogeochemical dynamics for coastal zones. Comparison of model output  
 307 to observational data by region and season is designed to document model skill at reproduc-  
 308 ing the statistics (e.g., mean values and variability) of ocean physical and biogeochemical  
 309 parameters at the spatio-temporal scales more relevant for evaluating human impacts on the  
 310 coastal environment. Comparison of model output to observational data for biogeochemi-  
 311 cal rates assures that model is capturing the appropriate transformations in nutrients and  
 312 carbon that structure the ecosystem response to eutrophication. Finally, the evaluation of  
 313 model behavior compared to the expected physical and biogeochemical dynamics for coastal  
 314 zones is a more qualitative evaluation of model performance to document that the model  
 315 broadly reproduces oceanographic phenomena in a way that reflects our understanding of  
 316 nearshore ocean environments.

#### 317 3.1 Description of Observational Datasets

##### 318 3.1.1 Ship-Based Ocean Monitoring

319 The SCB is home to a suite of long-running monitoring programs that make it one of  
 320 the best observed coastal ecosystems in the world (3, lower). Among them, the Califor-  
 321 nia Cooperative Oceanic Fisheries Investigations (CalCOFI) program (McClatchie, 2016),  
 322 initiated in the 1950s, samples the SCB quarterly each year, collecting hydrographic and

323 biogeochemical measurements in coordination with the Southern California Coastal Ocean  
324 Observing System (SCCOOS). These observations are augmented nearshore by quarterly  
325 surveys of nearshore water column and benthic parameters conducted collaboratively since  
326 1990 by POTW agencies as a part of their regulatory monitoring requirements (Howard  
327 et al., 2014; McLaughlin et al., 2018; Booth et al., 2014; Nezlin et al., 2018). These pro-  
328 grams provide good temporal and geographical coverage of both the offshore (CalCOFI)  
329 and nearshore (POTW) areas, coinciding with the model period, and include publicly avail-  
330 able water quality data for targeted sites measured quarterly. We validated model output  
331 against observed temperature, dissolved oxygen, nitrate, ammonium, chlorophyll, carbon  
332 system parameters (pH and aragonite saturation state), primary production, and nitrifica-  
333 tion.

334 *In situ* measurements have inherent uncertainty, due to a combination of measurement  
335 sensitivity and sampling frequency and intensity, making them an imperfect “truth”  
336 with which to compare to model output. However, this uncertainty is not the same for  
337 all parameters. Both temperature and dissolved oxygen are collected using high resolution  
338 probes, though the two programs used in this study incorporate slightly different calibra-  
339 tion protocols for dissolved oxygen, lending greater confidence to data-model comparisons  
340 for these datasets. Chlorophyll is measured on discrete bottle samples in the CalCOFI pro-  
341 gram, a high quality measurement, but inferred from *in situ* fluorescence measurements in  
342 the POTW monitoring program, adding uncertainty to these measurements. Nitrate and  
343 ammonium concentrations are measured on discrete bottle samples for both programs, but  
344 the detection limits are more sensitive in the CalCOFI program. Furthermore, nutrients are  
345 not measured with the same sampling density in POTW monitoring programs as sensor data.  
346 Similarly, primary production is measured at a subset of locations in the CalCOFI program  
347 and as a short-term special study in Southern California Bight Regional Marine Monitoring  
348 Program (Bight Program). Details on measurements and sample collection protocols for the  
349 CalCOFI program can be found on their website (<https://calcofi.org> ; McClatchie (2016))  
350 and for the POTW monitoring programs in Howard et al. (2014). We also use selected  
351 nutrient observations from the Santa Monica Bay Observatory (SMBO) mooring located  
352 in the Santa Monica Bay (Leinweber et al., 2009). Fig. 3 shows a map of all monitoring  
353 stations used in this study. The repository of data can be found in Kessouri, McLaughlin,  
354 et al. (2020).

### 355 **3.1.2 High Frequency Radar and Acoustic Doppler Current Profilers**

356 High Frequency Radar (HF) data from the database of the University of California, San  
357 Diego (<https://hfrnet-tds.ucsd.edu/thredds/catalog.html>) provide surface currents along the  
358 west coast of the United States, including the SCB. Seasonally averaged data from 2012-2020  
359 were used to analyze trends of surface currents in the Bight compared to the model. Acous-  
360 tic Doppler Current Profilers (ADCP) provide current data in the water column. ADCP  
361 measurement data from Orange County Sanitation District (OCSD) for the period June  
362 1999 to June 2000 and Los Angeles County Sanitation District (LACSD) during November  
363 2000 to June 2007 were used to validate vertical profiles of currents.

### 364 **3.1.3 Remote sensing observations**

365 Satellite ocean color measurements for chlorophyll were used to characterize horizontal  
366 gradients at finer scales and higher density than possible with the ship-based monitoring.  
367 We use monthly averaged surface chlorophyll concentration from the period 1997 to 2000  
368 derived from the SeaWiFS sensor at 4 km spatial resolution. Large gaps in the dataset  
369 can occur because of dense cloud cover that occurs in late spring and early summer. The  
370 products of the Vertically Generalized Production Model (VGPM) net primary production  
371 algorithm (Behrenfeld & Falkowski, 1997) were also considered for this validation. Despite  
372 limitations, satellite data provide a valuable representation of the spatial distribution of  
373 chlorophyll, temperature, and primary production at seasonal scales over the region.

374

### 3.2 Performance Statistics

375

376

377

378

379

380

381

382

383

384

385

386

387

Our approach to a statistical assessment of agreement between model predictions versus observations reflect the fact that the hydrodynamic model, under the influence of realistic forcings (e.g. wind fields) and without data assimilation, develops its own intrinsic variability in circulation, e.g. submesoscale eddies (McWilliams, 2007). The resulting modeled state variables would not necessarily overlap with observations on a point-by-point basis, but would be comparable to observations when averaged over appropriate spatio-temporal scales. We assessed a suite of statistics and metrics, following the methodology of Allen et al. (2007), to assess how well the model reproduces the magnitude and gradients of selected state variables, whether the model agreement has an apparent bias, and how well the model reproduces natural variability. We calculated six metrics, defined in the following, where  $N$  is the total number of appropriate observational data,  $D$  represents each individual observational datum,  $\bar{D}$  is the mean of the observational data,  $M$  is the model estimate representing an observation, and  $\bar{M}$  is the mean of the model estimate. The metrics considered include:

The Pearson correlation coefficient, reflecting the degree of linear correlation between the observed and model variable, and the statistical significance (p-value) of this correlation:

$$r_{xy} = \frac{\sum_{n=1}^N (D_n - \bar{D})(M_n - \bar{M})}{\sqrt{\sum_{n=1}^N (D_n - \bar{D})^2} \sqrt{\sum_{n=1}^N (M_n - \bar{M})^2}}; \quad (7)$$

The Cost Function (CF), which gives a non-dimensional value indicative of the goodness of fit between two sets of data, quantifying the difference between model results and measurement data:

$$CF = \frac{1}{N} \sum_{n=1}^N \frac{|D_n - M_n|}{\sigma_D} \quad (8)$$

388

where  $\sigma_D$  is the standard deviation of the observations;

The Bias (B) (the sum of model error normalized by the data):

$$B = \frac{\sum (D - M)}{\sum D}; \quad (9)$$

The Ratio of the Standard Deviations (RSD):

$$RSD = \frac{\sigma_D}{\sigma_M} \quad (10)$$

389

where  $\sigma_M$  is the standard deviation of model outputs;

The Nash-Sutcliffe Model Efficiency (ME) (Nash & Sutcliffe, 1970), a measure of the ratio of the model error to the variability of the data:

$$ME = 1 - \frac{\sum (D_n - M_n)^2}{\sum (D_n - \bar{D})^2}; \quad (11)$$

And the two-sample t-test, or Welch's t-test (Welch, 1947; Derrick et al., 2016):

$$H = (\bar{D} - \bar{M}) / \sqrt{\frac{\sigma_D^2}{N} + \frac{\sigma_M^2}{N}}. \quad (12)$$

390

391

We score the model performance following Table 1 per the methodology of Allen et al. (2007).

## 4 Model performance assessment findings

### 4.1 Ocean circulation

The SCB is situated at the confluence of water masses from the subarctic Pacific via the California Current, and from the eastern tropical North Pacific via the California Undercurrent, which all interact with the local topography, the coast, and the atmosphere to sustain variability in circulation on inter-annual, seasonal, and intraseasonal time scales (Dong et al., 2009; Bograd et al., 2015). The effects of this variability in circulation has profound consequences for coastal ocean biogeochemistry (Gruber et al., 2011; Bograd et al., 2015; Nagai et al., 2015; Nezlin et al., 2018), and is therefore critical that the model accurately simulates spatial and temporal variability in circulation patterns.

Fig. 4 shows the hydrodynamic characteristics of the SCB in the model compared to data. In the northern SCB, the model shows similar qualitative and quantitative patterns for the horizontal circulation compared to HF data (Fig. 4(a)-(b)) and as seen in Dong et al. (2009). The circulation in the SCB is characterized by northward currents in the first 20 km of the coast and cyclonic circulation in the middle of the SCB that is stronger in summer and weaker in winter. The model successfully reproduces observed current patterns, with similar current magnitudes. The intensity of the northward coastal branch of the current is on average about  $0.15\text{-}0.3\text{ m s}^{-1}$  in summer versus  $0.05\text{-}0.15\text{ m s}^{-1}$  in winter. The offshore southward branch is generally about  $0.3\text{ m s}^{-1}$  all year round (Fig. 4(a)-(b)). The dominant current in the coastal band (15 km from coast) of the SCB flows northward, and follows the topography along isobaths on the shelf (Fig. 4(g)-(h)).

The simulated June 1999-June 2000 variability of the current in depth is shown in the vertical profiles extracted off the coast of Palos Verdes and Orange county compared to the ADCP data at the same locations (Fig. 4(c)-(f)). The location of both of these profiles are a few kilometers from the continental slope and therefore capture a suite of physical processes, including mesoscale and submesoscale eddies, fronts, jets, and internal tides (Capet, McWilliams, et al., 2008; Kim et al., 2011; Dong et al., 2009). The model generally reproduces the means and range of the variability shown in these close to shore horizontal currents, which demonstrates that ROMS at  $dx = 0.3\text{ km}$  resolution captures the submesoscale variability described in Section 2.2.

In the northern SCB, cyclonic vortices are generated inside the Santa Barbara Channel (Fig. 4(i)) when the northward current that flows along the Ventura coast meets the eastern side of the Channel Islands, with higher intensity in summer (Fig. 4(a) versus (b)) (Winant et al., 2003). Submesoscale eddies are particularly prominent in this region, in particular persistent cyclonic eddies that drive an upward doming of isopycnals (Fig. 4(j)) (McGillicuddy Jr, 2016), which supplies nutrients to the euphotic layer. The model correctly reproduces this vertical transport, described in Brzezinski and Washburn (2011), and the high concentrations of nitrate and other nutrients in the upper layers of the Santa Barbara Channel, as further detailed in Section 4.3.1.

In the central and southern SCB (latitude  $< 34.7^\circ\text{N}$ ), the model successfully captures flow regimes around the large POTW outfalls, indicating that it can appropriately represent the dispersal of wastewater plumes in these regions. In the Santa Monica and San Pedro Bays, topography drives the circulation of currents inside the Bays, converging back to the main current offshore (Fig. 4(g)-(h)). On top of the Hyperion and JWPCP outfalls (in the Santa Monica Bay and offshore of the Palos Verdes peninsula, respectively), the current is mostly south-eastward. Near the OCSO outfall, the current direction varies in winter between south-eastward and north-westward, but is primarily southward in summer (Fig. 4(a)-(b), (e)-(f)). At the PLWTP outfall, the current is narrow, with a dominant south-eastern direction, parallel to the coast, demonstrated by both model and HF radar data.



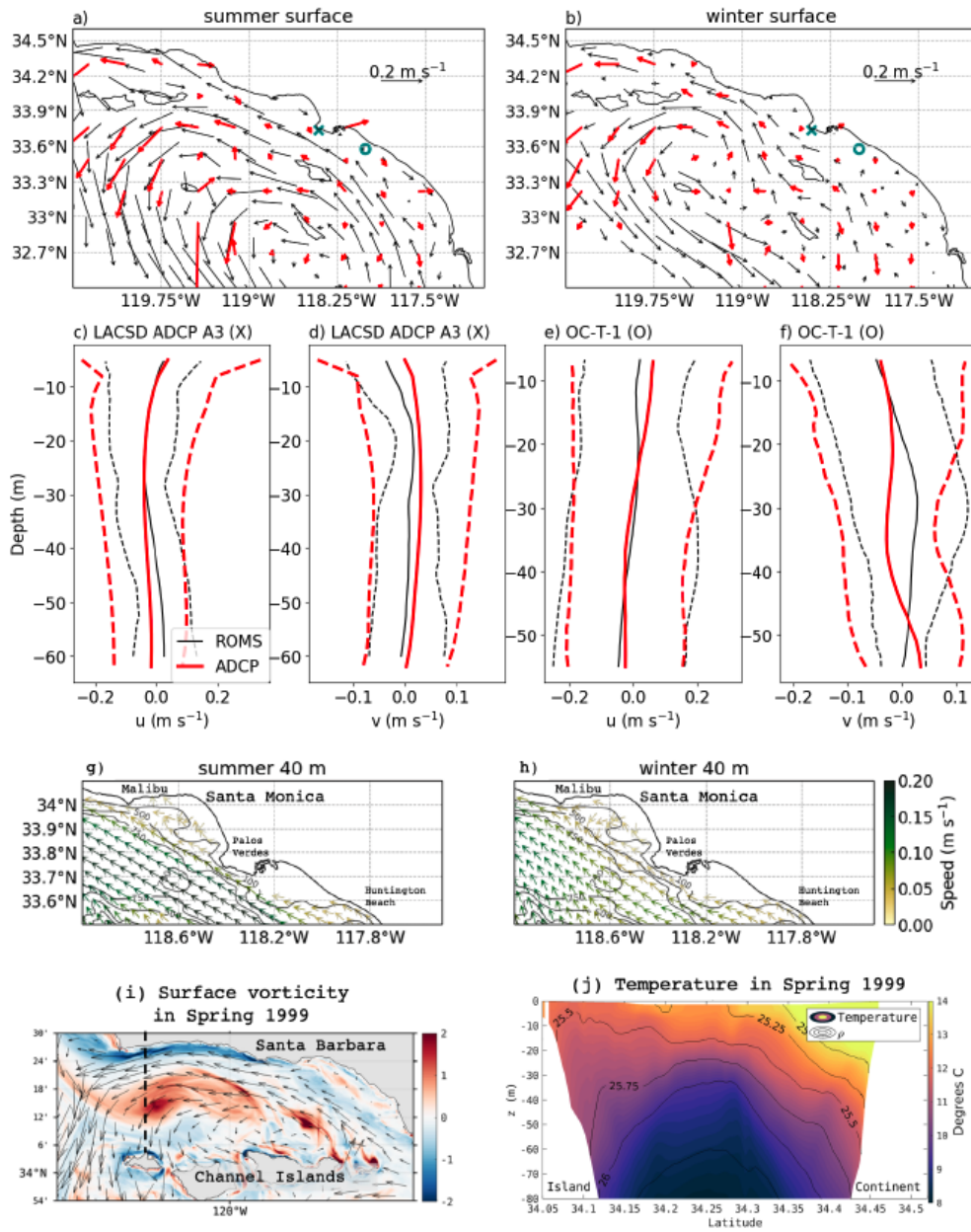


Figure 4: a) Mean surface currents in the Southern California Bight from HF data during 2012-2020 (thick red arrows) and model during 1999-2000 (black arrows) in summer and b) winter. c)-f) Vertical profiles of horizontal velocity components from ADCP instruments (thick red lines) and model (thinner black lines). The two dashed lines indicate the 5th and 95th percentile current values. c)-d) ADCP data come from the LACSD mooring A3 stationed at the teal ‘X’ in a)-b) and e)-f) come from the OCSD mooring OC-T-1 located at the teal ‘O’. g) Mean model current direction and speed (colored) at 40 m depth with bathymetry contoured in summer and h) winter. i) Surface model vorticity normalized by  $f$  in spring in Santa Barbara Channel showing cyclonic eddies. j) Cross-section of temperature and density isopycnals as drawn by the dashed line in (i) from model to show eddy-driven uplifting of the isopycnals in the center of Santa Barbara Channel.

442  
443

## 4.2 Vertical gradients and seasonal variability of temperature and mixed layer depth

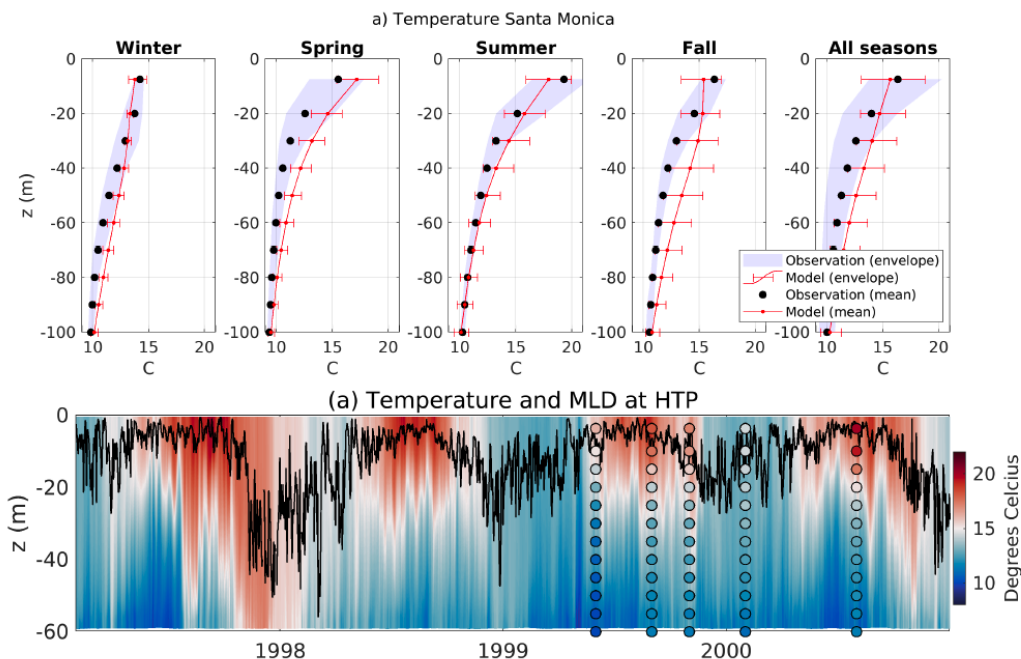


Figure 5: (a) Average seasonal profiles of temperature in the Santa Monica Bay. The red lines and red bars show the spatio-temporal mean and the variability from the model respectively. The black dots and the gray shading show the spatio-temporal mean and the variability from *in situ* data (City of LA stations), respectively. (b) Hovmöller diagram of temperature at the location of the Hyperion POTW outfall (HTP) in the Santa Monica Bay issued from the model. The black line shows the simulated time-series of mixed layer depth. The deepest mixing occurs during El Niño 1998 ( $>40$  m). Colored dots are average concentrations from *in situ* measurements.

444  
445  
446  
447  
448  
449  
450  
451  
452  
453  
454  
455  
456  
457  
458

The model successfully reproduces the three-dimensional and seasonal variability of physical tracers, here exemplified by temperature. Temperature is the parameter in which we have the highest confidence in the observational record, because observations are abundant, and sensors are accurate and precise, regularly calibrated, and with negligible drifts. The greatest source of observational uncertainty is temporal under-sampling, but some sources of model bias may also be important (e.g., from atmospheric forcing, wind, or shortwave detailed in Renault et al. (2021)). Quantitative statistical analysis indicates that model performance is *excellent* or *good* for nearly all metrics for all regions and seasons (see Table 2). The lowest performance of the model is characterized as *reasonable* for certain sub-regions (Palos Verdes, Orange County, and San Diego) in spring and fall (Palos Verdes only) (see Supporting Information Table S2). As noted above, this may be due to under-sampling during these months, which can be highly variable because the region is shifting between a well-mixed to a more stratified ocean regime. Detailed information on the other sub-regions and their statistical comparison can be found in the Supporting Information, Tables S1 to S4.

459  
460  
461

Following common practices (de Boyer Montégut et al., 2004), we define the mixed layer depth (MLD) as the depth at which temperature decreases from its surface value by more than  $0.2^{\circ}\text{C}$ . On average, the MLD deepens from the coast to offshore, and varies with season

| Statistic   | Excellent    | Good             | Reasonable       | Poor       |
|---|--------------|------------------|------------------|------------|
| Cost Function (Moll & Radach, 2003)                     | <1           | 1-2              | 2-3              | >3         |
| Nash-Sutcliff Model Efficiency (Nash & Sutcliffe, 1970) | >0.65        | 0.65-0.5         | 0.5-0.2          | <0.2       |
| Bias (Maréchal, 2004)                                   | < 0.1        | 0.1-0.2          | 0.2-0.4          | > 0.4      |
| H (Welch, 1947)   | 0            |                  |                  | 1          |
| Correlation Coefficient                                 | 1-0.9        | 0.9-0.8          | 0.8-0.6          | <0.6       |
| p-value   | <0.05        |                  |                  | >0.05      |
| Ratio of Standard Deviations                            | 1-0.9, 1-1.1 | 0.9-0.8, 1.1-1.2 | 0.8-0.6, 1.2-1.4 | <0.6, >1.4 |

Table 1: Summary of statistical tests of model performance and their interpretation used in this paper.

Santa Monica: Temperature

|             | H   | Correlation Coefficient | p-value | Cost Function | Bias    | Ratio of Standard Deviations | Nash-Sutcliffe Model Efficiency | Number of observations |
|-------------|-----|-------------------------|---------|---------------|---------|------------------------------|---------------------------------|------------------------|
| Winter      | 0 E | 0.96 E                  | 7E-06 E | 0.05 E        | -0.04 E | 1.10 G                       | 0.81 E                          | 716                    |
| Spring      | 0 E | 0.98 E                  | 8E-07 E | 0.10 E        | -0.10 G | 0.78 R                       | 0.51 G                          | 716                    |
| Summer      | 0 E | 0.97 E                  | 9E-06 E | 0.04 E        | -0.02 E | 1.07 E                       | 0.93 E                          | 712                    |
| Fall        | 0 E | 0.89 G                  | 3E-06 E | 0.09 E        | -0.08 E | 0.98 E                       | 0.51 G                          | 718                    |
| All Seasons | 0 E | 0.95 E                  | 3E-05 E | 0.08 E        | -0.07 E | 1.02 E                       | 0.73 E                          | 2862                   |

Table 2: Statistical comparison between *in situ* data and model outputs for temperature profile in Santa Monica Bay (City of LA stations). Letters next to numbers indicate model performance: E = Excellent, G = good, R = reasonable, P = Poor.

462 (e.g. in Santa Monica Bay in Fig. 5b). The model successfully simulates the seasonal cycle  
463 of MLD along the coast. For example, the model recreates the observed seasonal deepening  
464 of the mixed layer in the Santa Monica Bay to depths greater than 16-20 m (the typical  
465 depth of the upper signature of the POTW plumes, see Section 4.3.2) nearly every winter  
466 (black line in the Fig. 5b).

467 Regular winter shows a homogeneous upper layer of  $< 14^{\circ}\text{C}$  temperature, and a mixed  
468 layer located at 18-20 m in the coastal region and 40-60 m offshore. The surface ocean is  
469 colder around the Channel Islands ( $\text{SST} < 12^{\circ}\text{C}$ ) (see Fig. 19). In the open ocean, the model  
470 reproduces the de-stratification with deepening of the thermocline to about 70m and a MLD  
471 at about 40m (Fig. 6c and d). In summer, stratification is the strongest, reflecting an intense  
472 vertical temperature gradient, and the MLD (both in the model and in the observations) is  
473 found few meters below the surface (approximately 10 m). Temperature varies rapidly from  
474 more than  $20^{\circ}\text{C}$  at the surface in the southern domain ( $16\text{-}17^{\circ}\text{C}$  in the northern domain)  
475 to less than  $12^{\circ}\text{C}$  at 50m depth over the entire SCB (see also Fig. 19). In the open ocean,  
476 the model succeeds in reproducing the stratification that brings the seasonal thermocline to  
477 50m and the MLD to 15m (Fig. 6c) and e)).

478 The model reproduces interannual variability in MLD under the influence of El Niño-  
479 Southern Oscillation (ENSO, hereafter referred to as El Niño, i.e., the period from fall 1997  
480 to spring 1998 in Fig. 5b), when the MLD reached 40 m. We show that during winter of  
481 El Niño year, the entire water column of the SCB is warmer than on average, and surface  
482 temperature is more homogeneous, varying between  $15.5$  and  $17^{\circ}\text{C}$  (Fig. 6a). In the open  
483 ocean, during El Niño, with warmer upper layer than regular winters, the model shows  
484 good performance in reproducing the deepening of the seasonal thermocline ( $>120$  m) and  
485 of the MLD ( $>50$  m) (e.g. offshore Santa Monica Bay in Fig. 6a and b). These patterns of  
486 variability in temperature are consistent with regional observations of El Niño in the SCB  
487 (Todd et al., 2011).

### 488 4.3 Dissolved Inorganic Nitrogen

#### 489 4.3.1 Spatial patterns and seasonality of nitrate

490 Nitrate observations are only broadly available in the offshore CalCOFI dataset, so  
491 only large-scale regional patterns in nitrate concentration can be validated. There is a clear  
492 seasonality of nitrate, where surface concentrations are higher in spring and summer, and  
493 decrease in fall and winter (Fig. 7). The model reproduces the average seasonal patterns  
494 observed in the *in situ* nitrate data across multiple regions. The model also captures along-  
495 shore variability in coastal nitrate concentrations, reproducing values greater than  $25$   $\text{mmol}$   
496  $\text{N m}^{-3}$  off Santa Barbara,  $20$   $\text{mmol N m}^{-3}$  off Los Angeles, and  $15$   $\text{mmol N m}^{-3}$  off San  
497 Diego.

498 The model also reproduces observed patterns in the depth of the nitracline (Mantyla  
499 et al., 2008; Nezlin et al., 2018), which tends to follow sloping density surfaces in the  
500 region. These patterns include: the high values at the euphotic depth limit ( $\sim 50\text{m}$  below  
501 the surface) along the Santa Barbara coast in spring; the doming of the nitracline in the  
502 center of the Santa Barbara Channel (Fig. 7b); the 20 to 30 m deep nitracline along the  
503 Los Angeles coast; and the deepening of the nitracline from about 30 m at the coast to  
504 more than 60 m offshore in San Diego. In the offshore region of the SCB, the model is  
505 consistent with observations showing high nitrate ( $>20$   $\text{mmol N m}^{-3}$ ) around the Channel  
506 Islands (not shown) as compared to less than  $5$   $\text{mmol N m}^{-3}$  farther offshore. This pattern  
507 is strongest in winter and summer, when the offshore regions are particularly oligotrophic  
508 (surface  $\text{NO}_3^- < 1$   $\text{mmol m}^{-3}$ ) throughout the SCB.

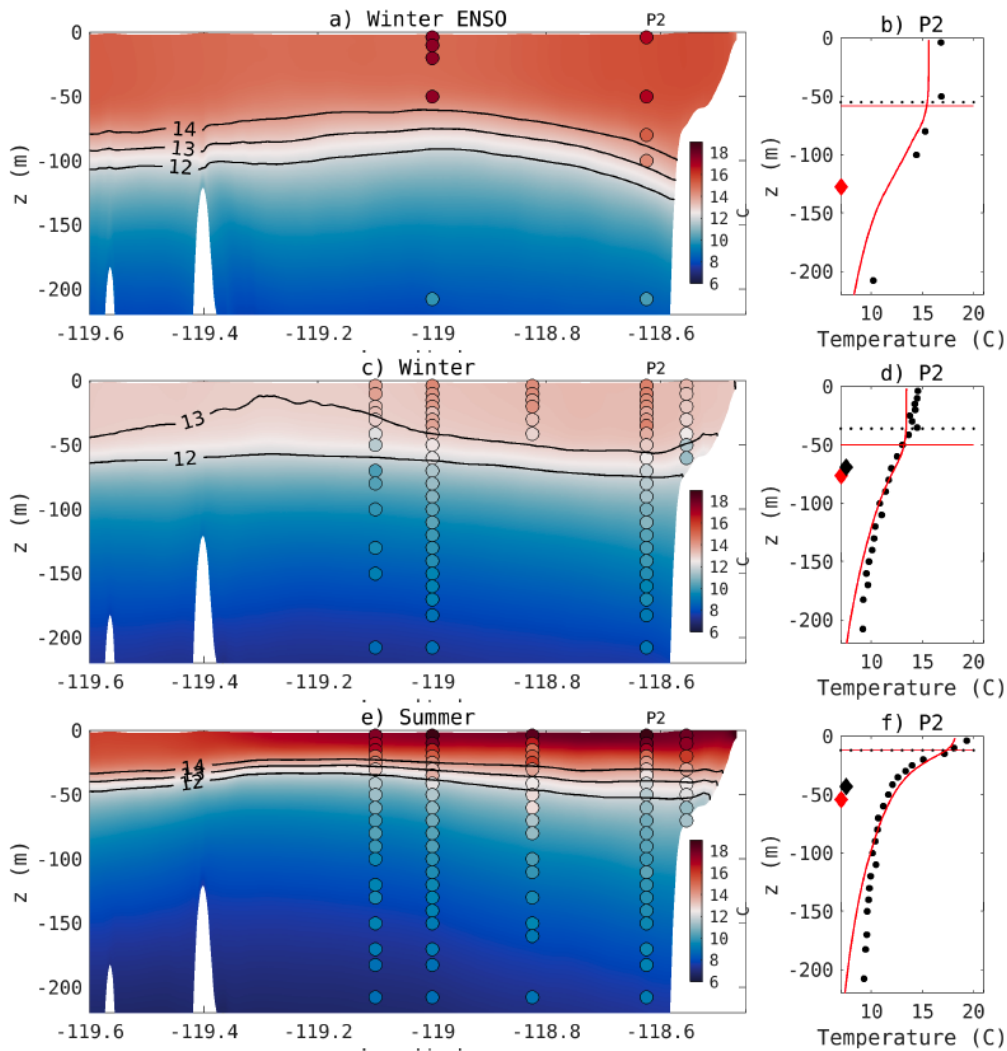


Figure 6: (a) Cross section of average temperature following line 86.7 from CalCOFI monitoring stations during an El Niño winter (12/1997 to February 1998). (b) Profile at station P2. Black dots are CalCOFI *in situ* data, red line is the simulated profile. The horizontal line is the MLD (black is CalCOFI, red is simulated). Diamonds (black is CalCOFI, red is simulated) is the depth of the maximum gradient to estimate the depth of the seasonal thermocline at 12°C. (c-d) are similar to (a-b) for average winter, and (e-f) are for average summer.



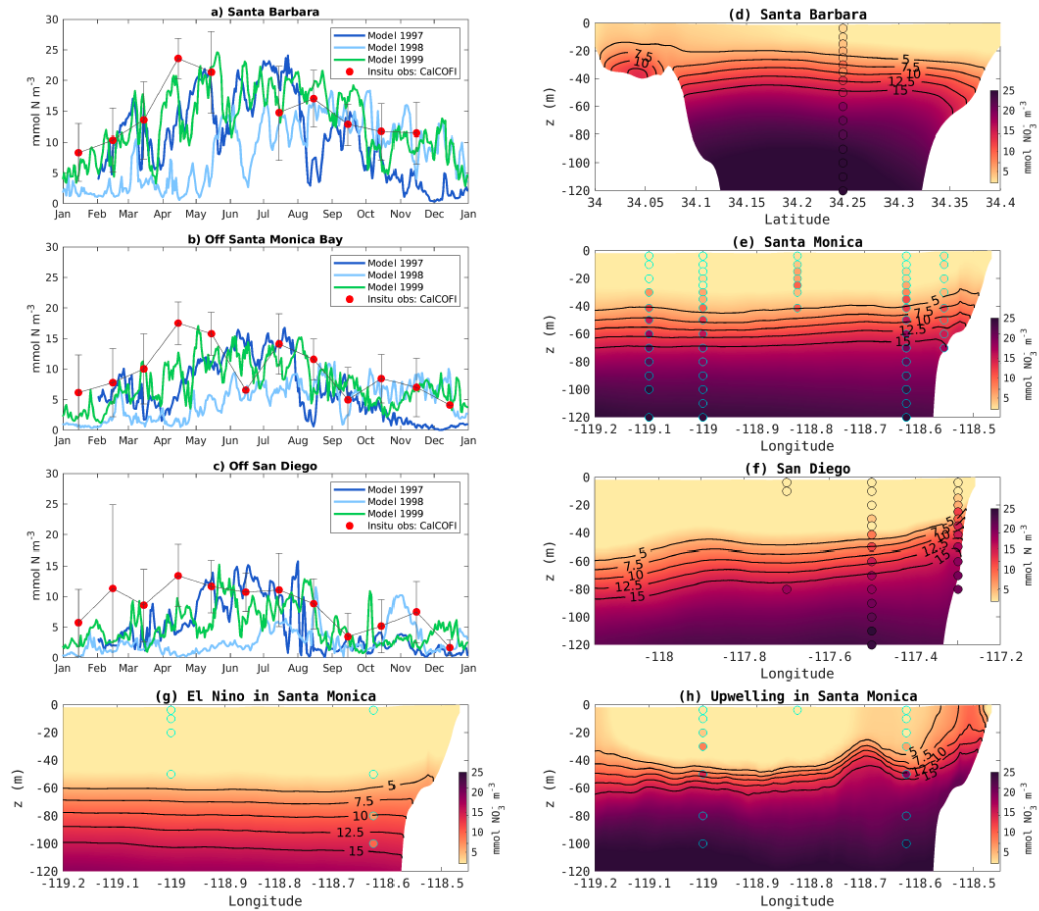


Figure 7: (a-c) Time series of nitrate concentration at 50 m depth in three different locations of the SCB: (a) is near the center of Santa Barbara Channel, (b) is offshore the Santa Monica Bay, and (c) is offshore San Diego. Model outputs are represented by the lines for three different years, with the dots showing mean values from *in situ* measurement from CalCOFI, and gray bars the standard deviation from the mean. The time-series show prominent interannual variability in addition to seasonal variability. While the years 1997 and 1999 show similar nitrate distributions, the El Niño period between the end of 1997 to 1998 is significantly different, showing nearly uniform concentrations between November 1997 through May 1998. This is caused by the deepening of the thermocline during El Niño, which depresses the nutricline. (d-f) Cross sections showing the average springtime nitrate concentration in (d) the Santa Barbara region (e) the SM region, and (f) the SD region. Background are model outputs and dots are CalCOFI *in situ* measurements. Model and *in situ* data agree on the vertical and seasonal patterns in the three regions. They highlight the main differences in these three regimes, consisting of a shallower nitracline in the Santa Barbara Channel, and a deeper nitracline in southern waters. (g-h) Comparison of nitrate concentrations during (g) winter El Niño (January-March 1998) and (h) during an upwelling event (the first week of May 1999) to illustrate the ability of the model (vs. *in situ* CalCOFI data) to simulate the vertical displacement of the nitracline during these specific events.

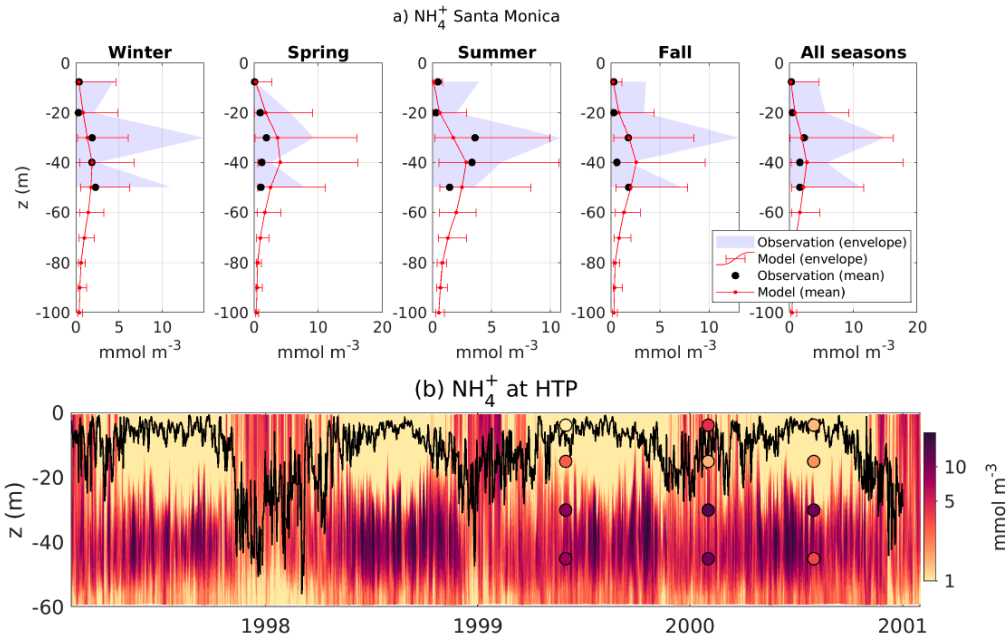


Figure 8: As for Fig. 5, but for ammonium concentration. These profiles are showing agreement on intensity, seasonality and shape of the vertical profile with exceptionally high concentrations at mid-depth.

Santa Monica: Ammonium

|             | H   | Correlation Coefficient | p-value | Cost Function | Bias    | Ratio of Standard Deviations | Nash-Sutcliffe Model Efficiency | Number of observations |
|-------------|-----|-------------------------|---------|---------------|---------|------------------------------|---------------------------------|------------------------|
| Winter      | 0 E | 0.94 E                  | 0.06 P  | 0.54 E        | 0.24 R  | 1.86 P                       | 0.68 E                          | 20                     |
| Spring      | 0 E | 0.85 G                  | 0.14 P  | 0.58 E        | -0.57 P | 0.69 R                       | -0.61 P                         | 21                     |
| Summer      | 0 E | 0.58 P                  | 0.42 P  | 0.72 E        | 0.19 G  | 1.76 P                       | 0.29 R                          | 21                     |
| Fall        | 0 E | 0.91 E                  | 0.09 P  | 0.42 E        | 0.07 E  | 1.47 P                       | 0.80 E                          | 21                     |
| All Seasons | 0 E | 0.81 G                  | 0.10 P  | 0.36 E        | -0.03 E | 1.23 R                       | 0.60 G                          | 83                     |

Table 3: Statistical comparison between *in situ* data and model outputs for ammonium profile in Santa Monica Bay.

### 4.3.2 Vertical gradients and seasonal variability of ammonium

Ammonium concentrations above a natural background concentration of  $1 \text{ mmol N m}^{-3}$  are indicative of POTW wastewater plumes. The model reproduces the observed average vertical profile of ammonium in the Santa Monica Bay, falling within the range of observed variability (Fig. S8a). Similar figures for other regions are shown in the Supporting Information (Fig. S6-Fig. S9). All regions show a similar maximum concentration between 30 to 45 m below the surface, in all seasons. The highest concentrations are seen in summer, when stratification is stronger, while lower concentrations in winter likely reflect increased dilution by seasonal mixing from the deepening of the mixed layer (Fig. 8b). Near ocean outfalls, both model and observations show mid-depth peaks of ammonium concentration, occasionally exceeding  $10 \text{ mmol m}^{-3}$ , which considerably overshadow values observed away from outfalls. In the model, these high ammonium concentrations are caused by wastewater plumes.

The main source of uncertainty in data-model comparisons is the limited spatial and temporal coverage of measurements. Ammonium is typically measured near ocean outfalls and is therefore biased towards high concentrations, but the dataset is highly variable. Methodological difficulties exist with the measurement of ammonium in seawater, and as such, we excluded non-detectable ammonium values in our analyses. Near the submarine outfalls, ammonium concentrations are likely extremely heterogeneous due to buoyant plume filaments, as observed in DiGiacomo et al. (2004) and in Warrick et al. (2007) in the Santa Monica Bay, as well as in other regions (e.g. Florida, in Marmorino et al. (2010)) and in idealized case studies (e.g. Ho et al. (2021)). These plume filaments are caused by horizontal advection and straining of the discharged effluent by currents. As a result, the under-sampling of ammonium may have led to poor statistical agreement between observations and model output. The model shows high to moderate agreement for the shape of the profile and the mean concentration (Table 3). However, p-values for the correlations were not always significant. Similarly, there were often biases and low performance regarding variability statistics. This low model performance can be explained by the following two reasons: (1) spatial sampling is likely missing plume filaments, for example observational data points with high ammonium values that are capturing the plume are recorded next to very low or non-detectable values; and (2) the resolution of the model (0.3 km), as well as model averaging over the day, season, and depth range causes plume filaments to appear more uniformly spread near the outfalls. Because plume filaments are lost in this averaging, the model represents plumes as cloud-like distributions around outfalls; nevertheless, the average ammonium concentration of wastewater plumes is reasonably well represented. Detailed information on the other sub-regions and their statistical comparison can be found in the Supporting Information Tables S1 to S4.

### 4.3.3 Horizontal gradients of ammonium

Both *in situ* observations (dots in Fig. 9, Fig. 8a) and model output (background colours in Fig. 9 and red line in Fig. 8a) show high concentrations of ammonium in the subsurface layer below the thermocline (Fig. 9c), which we refer to as "high-ammonium plume". This high-ammonium plume can extend from Huntington Beach to South Ventura, encompassing three of the four major wastewater treatment plant outfalls in the SCB (See Section 2.4). Both model and observations show that the width and strength of the high-ammonium plume are greatest in summer compared to other seasons. The Santa Monica Bay Observatory mooring (SMBO, Leinweber et al. (2009)) located 17 km north-west of the submarine pipe Hyperion in Santa Monica Bay (Fig. 9g) frequently recorded concentrations higher than  $2 \text{ mmol m}^{-3}$ , and up to  $4 \text{ mmol m}^{-3}$  at mid-depth (Fig. 9e), consistent with the model (Fig. 9f). The depth of the maximum variability is at 40 m in the model, and slightly shallower in the SMBO data, possibly because of a mismatch in the time period (1997-2000 for the model, and 2004-2010 for the SMBO). During winter, the model indicates vertical mixing and dilution of the plume at the surface. Accordingly, ammonium concentrations

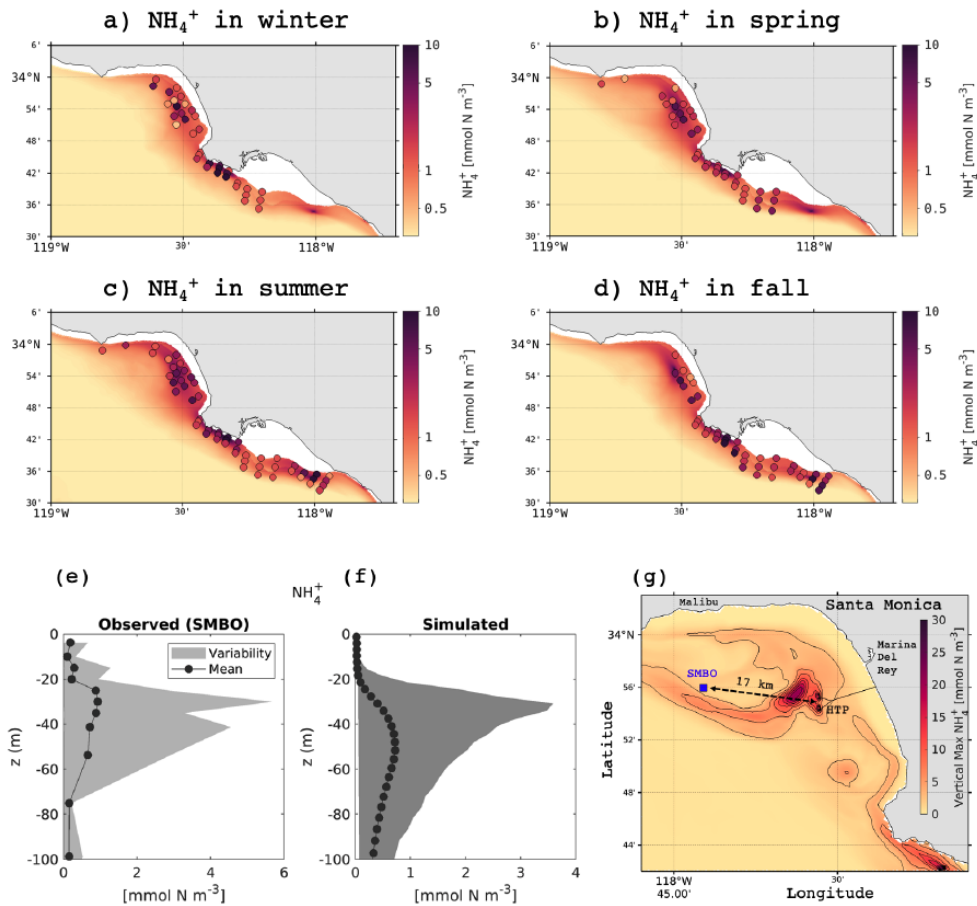


Figure 9: (a-d) seasonal average ammonium concentration between 30 and 45 m depth from the model, and dots from observations. High values highlight the movement and dispersion of subsurface wastewater plumes along the Orange and Los Angeles counties. The highest concentrations are located within a narrow coastal band of about 10 - 15 km width, and are carried along the topography by the mean currents. (e-f) show a statistical comparison of the vertical profiles of ammonium at the SMBO mooring and the same location in the model. The anthropogenic ammonium plume signature is apparent, albeit intermittently, 17 km away from the Hyperion outfall. (g) shows the simulated vertical maximum concentration of  $\text{NH}_4^+$  averaged during a representative day to illustrate the dispersal of the effluent toward SMBO originating from the 2 diffusers of Hyperion Treatment Plant (HTP).

561 decrease slightly at depth (Fig. 9a) and increase at the surface, reaching values up to 2-6  
562  $\text{mmol m}^{-3}$ , also consistent with observations around the outfall pipes (Fig. 8a).

#### 563 **4.3.4 Spatial patterns in rates of nitrogen transformation**

564 Although we had no *in situ* nitrogen transformation rates with which to compare model  
565 output during the simulation period, several datasets exist for the region that can serve  
566 as a test for whether the model is simulating reasonable patterns in rates via the right  
567 mechanisms. We found that modeled rates do agree with observed nitrogen transformation  
568 rates. Nitrification rates, the sequential oxidation of  $\text{NH}_4^+$  to  $\text{NO}_3^-$  via  $\text{NO}_2^-$ , have been  
569 observed to be higher within wastewater plumes in the SCB (McLaughlin et al., 2021), a  
570 pattern driven by high ammonium concentrations in the discharges (McLaughlin, Nezhlin, et  
571 al., 2017). In both observations and the model, nitrification predominately occurs below the  
572 euphotic layer. Modeled vertically-integrated nitrification rates vary between 0.15 and 1.5  
573  $\text{mmol N m}^{-2}\text{d}^{-1}$ , consistent with observations within the SCB and in the California Current  
574 (Table 5). The model also reproduces higher nitrification rates within wastewater plumes  
575 (See Supporting Information Fig. S22). There is also good agreement between observed and  
576 modeled rates of nitrate and ammonium uptake by phytoplankton communities (McLaughlin  
577 et al., 2021) and (Kudela et al., 2017). Modeled nitrate uptake rates vary between 2 and 11  
578  $\text{mmol N m}^{-2}\text{d}^{-1}$  and ammonium uptake rates vary between 6 and 51  $\text{mmol N m}^{-2}\text{d}^{-1}$  in  
579 the Los Angeles and Orange County coasts, consistent with observations in the SCB (Table  
580 5).

#### 581 **4.4 Chlorophyll concentrations**

582 In general, the model was found to reproduce vertical and horizontal gradients in chloro-  
583 phyll concentration in different subregions (Fig. 12). The timing of blooms was consistent  
584 with changes in mixing and nutrient delivery in the SCB. We present three different subre-  
585 gions characterized by distinct hydrodynamic regimes: the Santa Barbara Channel, the Los  
586 Angeles coast, and San Diego coast.

587 There are several sources of uncertainty in the chlorophyll, primary production, phyto-  
588 plankton growth, and grazing rates observational records. For chlorophyll, bottle measure-  
589 ments are accurate and precise, but measure a limited portion of the water column. Sensors  
590 are accurate and precise in their measurement of fluorescence and have a rapid response  
591 time, providing vertically resolved profiles; however, the algorithm to convert fluorescence  
592 to chlorophyll concentration is inaccurate for the SCB. As a result, a correction factor has  
593 been applied to Bight data which adds uncertainty to the observational dataset (Nezhlin et  
594 al., 2018). Satellite measurements of chlorophyll are inferred from ocean color (Kahru et  
595 al., 2009). This method works well offshore, but breaks down nearshore where terrestrially-  
596 derived colored dissolved organic matter creates uncertainty in reported satellite chlorophyll  
597 estimates on the order of 100% or greater (Zheng & DiGiacomo, 2017). For primary pro-  
598 duction, the incubation method to derive the rates is sensitive and precise (Cullen, 2001),  
599 though measured rates are subject to bottle effects and there is some ambiguity as to whether  
600 the experiments measure net primary production or gross primary production (Regaudie-de  
601 Gioux et al., 2014). Phytoplankton growth and zooplankton grazing are also determined  
602 experimentally, and duplicate measurements indicate that these methods are not very pre-  
603 cise, with differences between duplicates ranging from 80% to 200% (Landry et al., 2009; Li  
604 et al., 2011). For all three measurements, spatial and temporal under-sampling, particularly  
605 during seasons with high variability, adds uncertainty to the data-model comparison.

#### 606 **4.4.1 Horizontal gradients in chlorophyll**

607 Despite the uncertainties outlined above, the model successfully simulates horizontal  
608 gradients in chlorophyll in the three subregions (Santa Barbara, Los Angeles and San Diego).  
609 The model captures the early, wide-spread spring bloom in the Santa Barbara Channel,



610 which occurs as a combination of a coastal bloom driven by spring upwelling, followed by a  
611 bloom in the central and southwestern regions of the Channel (near the islands) in spring  
612 and summer (Fig. 10). The latter is driven by the strengthening of the cyclonic circulation  
613 in the Channel, which transports nutrients to the upper layers, and is regularly observed in  
614 the region (Brzezinski & Washburn, 2011). The model captures the strong seasonality in  
615 chlorophyll, wherein concentrations change from near zero in winter to up to  $8 \text{ mg Chl m}^{-3}$  in  
616 spring. Of the three regions, the blooms off Santa Barbara extends further into late summer  
617 and fall, where the average concentration is approximately  $1\text{-}2 \text{ mg Chl m}^{-3}$ , a pattern  
618 replicated in both model and observations. Spatially, the model correctly reproduces the  
619 main patterns observed in satellite-based reconstructions, with spatial correlation coefficient  
620 varying between 0.5 and 0.9, and a cost-function demonstrating excellent scores. The bias is  
621 also excellent ( $<0.05$ ) in all seasons except winter, when it is reasonable, potentially because  
622 of weaker spatial gradients than observed.

623 In the Los Angeles subregion, the model predicts broad patterns in chlorophyll concentra-  
624 tions with good spatial correlation coefficients across the seasons (0.75 to 0.89), including  
625 a persistent bloom in the San Pedro Bay, consistent with in situ observations (Nezlin et al.,  
626 2012), and remote sensing (Fig. 11). Spatially, the cost-function shows excellent scores  
627 across all seasons, and the bias is good to reasonable. Both satellite-derived and modeled  
628 chlorophyll show concentrations in the San Pedro Bay consistently higher than  $3 \text{ mg Chl}$   
629  $\text{m}^{-3}$  year-round, often extending into the Santa Monica Bay. The model also reproduces  
630 the strong offshore gradients in chlorophyll, where across less than 15 km offshore surface  
631 concentrations are reduced 3 to 4 fold ( $<1 \text{ mg Chl m}^{-3}$ ) further decreasing towards the open  
632 ocean. The model also reproduces the timing and magnitude of the blooms in the Santa  
633 Monica and San Pedro Bays. The difference in timing of maximum chlorophyll concentra-  
634 tions between the Santa Monica and San Pedro Bays likely reflects differences in nutrient  
635 supply. Nutrients, in particular ammonium, are available near the surface during winter  
636 (see Section 4.3.2), reflecting more vigorous mixing of the wastewater plume and land-based  
637 nutrient supply by rivers (in particular in the San Pedro Bay) during winter storms (Lyon  
638 & Stein, 2009). Storms and winter mixing events have been connected to phytoplankton  
639 blooms in the region (Nezlin et al., 2012; Mantyla et al., 2008). Further offshore in the Los  
640 Angeles region, the model recreates the weak seasonality of surface chlorophyll, with higher  
641 concentrations during winter and spring, and lower concentrations in summer and fall. In  
642 the offshore region of the Santa Monica Bay, the seasonal cycle is marked by the increase  
643 of surface phytoplankton between March and May as shown in Fig. 12b. Mean chlorophyll  
644 values reach up to 3 to  $4 \text{ mg Chl m}^{-3}$  in April and May, although concentrations below  $2$   
645  $\text{mg Chl m}^{-3}$  are more common, consistent with observations over the same period.

646 Offshore of the San Diego coast, the model recreates a slight increase in surface chloro-  
647 phyll in March; however, concentrations are generally below  $1 \text{ mg Chl m}^{-3}$  year-round (Fig  
648 12(c)). The oligotrophic conditions of the southern Bight (Nezlin et al., 2012; Mantyla  
649 et al., 2008) have been attributed to a deeper nitracline, which in turns supports a deep  
650 chlorophyll maximum layer (Mantyla et al., 2008). This feature is well represented in the  
651 model, which reproduces relatively high concentrations of chlorophyll in subsurface layers  
652 (generally between 20 and 90 m depth in the region).

#### 653 **4.4.2 Vertical gradients and seasonal variability of chlorophyll**

654 The goodness-of-fit statistical metrics (correlation coefficient and cost function) for  
655 chlorophyll are generally *excellent* or *good* for most seasons for all sub-regions (Table 4).  
656 We were most concerned with performance for these metrics because the remaining statistics  
657 may be affected by the aforementioned uncertainties due to the fluorometry calibration. The  
658 observational measurements should be internally consistent (if not accurate), so the shapes  
659 of profiles should be "correct" even if the magnitude is off due to poor calibration, and  
660 the model was able to replicate these shapes accurately. Despite calibration issues, the model  
661 reproduced chlorophyll reasonably well for the northern Bight sub-regions of Santa Monica

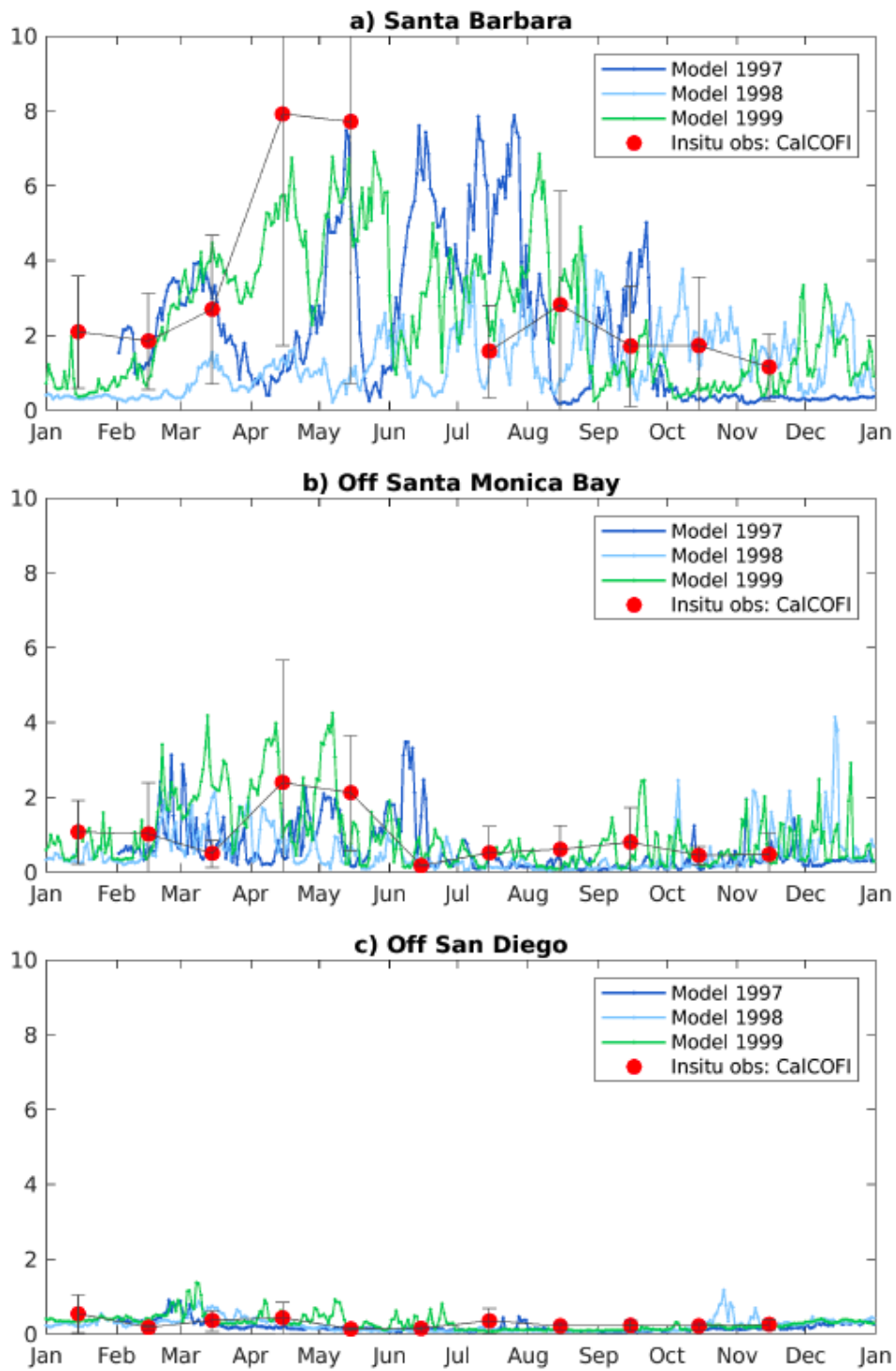


Figure 10: Comparison of seasonally-averaged surface chlorophyll between SeaWiFS remote sensing data (left panels) and the model (right panels) in the Santa Barbara Channel, where an important seasonal bloom is observed. The 3 numbers numbers for each season represent statistics of spatial comparison between the observed and simulated chlorophyll: Pearson's correlation ( $R$ ), cost function ( $C$ ) and bias ( $B$ ).

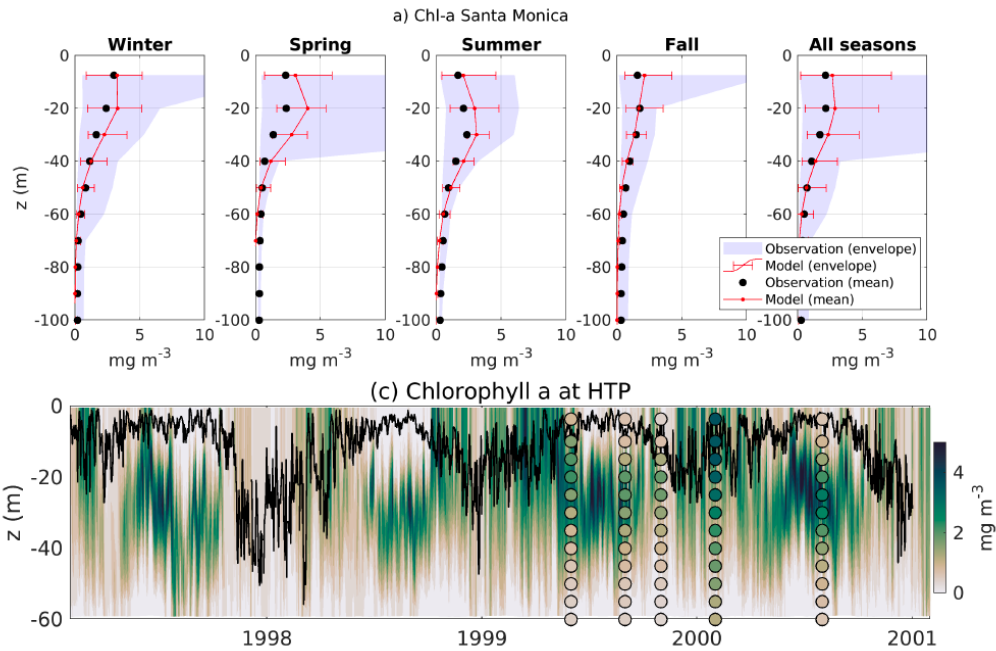


Figure 11: Comparison of seasonally-averaged surface chlorophyll between SeaWiFS remote sensing data (left panels) and the model (right panels) for years 1998-2000 in the Santa Monica and San Pedro Bays, where major POTW outfalls are found. The figure highlights the persistent coastal phytoplankton bloom, and the sharp inshore-offshore gradients. The 3 numbers for each season represent statistics of spatial comparison between the observed and simulated chlorophyll: Pearson's correlation (R), cost function (C) and bias (B).

Santa Monica: chlorophyll

|             | H   | Correlation Coefficient | p-value | Cost Function | Bias    | Ratio of Standard Deviations | Nash-Sutcliffe Model Efficiency | Number of observations |
|-------------|-----|-------------------------|---------|---------------|---------|------------------------------|---------------------------------|------------------------|
| Winter      | 0 E | 0.99 E                  | 9E-06 E | 0.48 E        | 0.09 E  | 0.91 E                       | 0.94 E                          | 714                    |
| Spring      | 0 E | 0.93 E                  | 9E-05 E | 0.90 E        | -0.42 P | 0.52 P                       | -0.49 P                         | 716                    |
| Summer      | 0 E | 0.99 E                  | 1E-08 E | 0.58 E        | -0.07 E | 0.60 R                       | 0.47 R                          | 712                    |
| Fall        | 0 E | 0.99 E                  | 8E-08 E | 0.48 E        | 0.16 G  | 0.75 R                       | 0.76 E                          | 718                    |
| All Seasons | 0 E | 0.99 E                  | 4E-08 E | 0.50 E        | -0.01 E | 0.73 R                       | 0.80 E                          | 2860                   |

Table 4: Statistical comparison between *in situ* data and model outputs for chlorophyll profile in Santa Monica Bay.

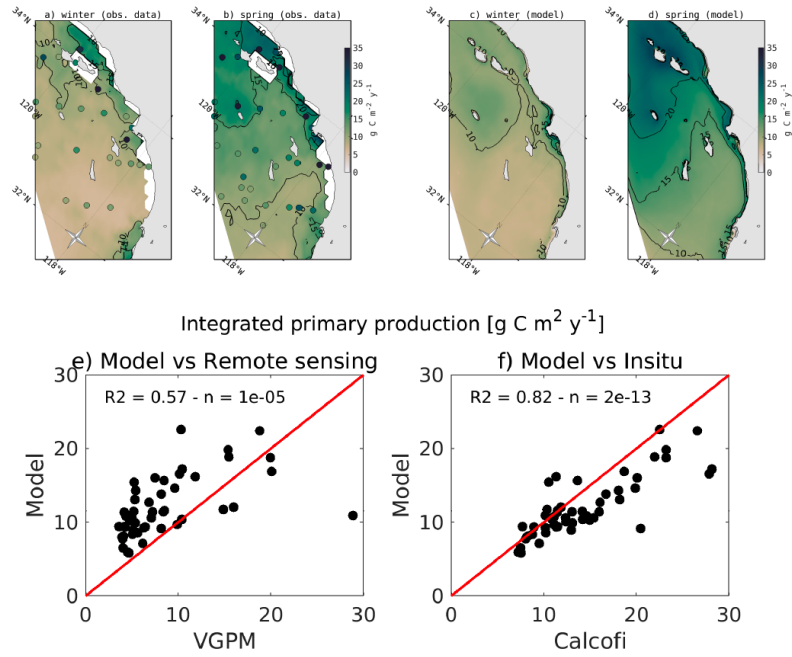


Figure 12: Comparison of surface chlorophyll concentration between different years of model output, and a climatology from CalCOFI *in situ* data. (a) is near the center of Santa Barbara Channel, (b) is offshore the Santa Monica Bay, and (c) is offshore San Diego. The model reproduces different productivity regimes across the Southern California Bight, with highly productive waters in the northern region, where average concentrations greater than  $3 \text{ mg m}^{-3}$  are observed for more than half of the year, and oligotrophic southern regions, where average surface concentrations rarely exceed  $1 \text{ mg m}^{-3}$ .

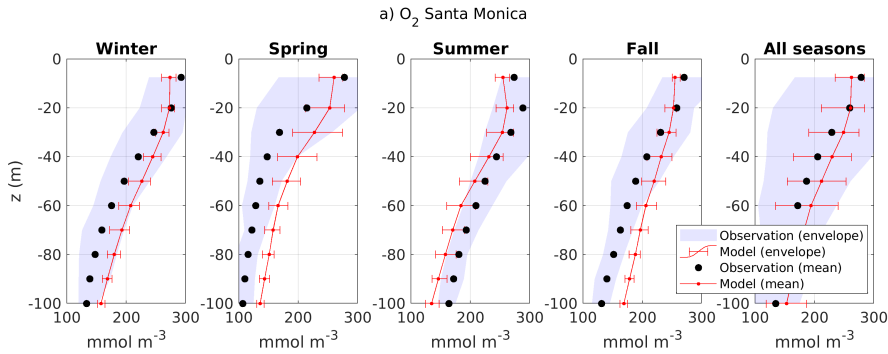


Figure 13: As for Fig. 5, but for chlorophyll concentration. Vertical profiles show a good agreement between simulated and *in situ* data, and display the formation of a subsurface chlorophyll maximum in summer, and a surface maximum in winter and spring. Concentrations in winter vary up to  $+5 \text{ mg Chl m}^{-3}$ . Note the very low concentrations during 1998 El Niño in the entire water column.

662 Bay (Fig. 13) and Ventura/Oxnard (Supporting Information Fig. S11). Similar figures for  
663 other regions are shown in the Supporting Information (Fig. S10 - Fig. S13). All show that  
664 the model is reproducing the magnitude and general shape of observed profiles. However, the  
665 model did not capture the variability for most regions (except for Palos Verdes), generally  
666 scoring *reasonable* or *poor* in the ratio of standard deviations for most seasons, particularly  
667 spring. This is likely a result of the spatial and temporal averaging. Chlorophyll is highly  
668 variable in space and time and under-sampling in either of these dimensions will adversely  
669 affect variability estimates for a region and season. Therefore, reasonable performance for  
670 these metrics was not unexpected. This suggests that the model may provide a conservative  
671 estimate of phytoplankton biomass in the southern Bight, while reproducing accurate spatial  
672 and temporal patterns in that biomass.

673 In addition to transporting nutrients from depth, upwelling 'seeds' surface waters with  
674 subsurface water masses dominated by selected phytoplankton species, stimulating surface  
675 blooms near the coast (Seegers et al., 2015). The model successfully reproduces this process,  
676 wherein the subsurface chlorophyll maximum shoals and intensifies in spring, forced by the  
677 vertical movement of the thermocline driven by upwelling. This seasonal dynamics occurs  
678 across the domain in the model.

679 Offshore, in the more oligotrophic portion of the SCB, the model predicts that more  
680 than 60% of the maximum concentration of phytoplankton biomass remains below the sur-  
681 face year-round, constantly fed by subsurface nutrients injections. This is consistent with  
682 observations of a deep chlorophyll maximum throughout the region (Nezlin et al., 2018;  
683 Mantyla et al., 2008; Seegers et al., 2015), and with observations at the San Pedro Oceanic  
684 Time-Series (SPOT) located between the Palos Verdes Peninsula and Catalina Island (Fig.  
685 3, lower panel). At SPOT, a region weakly influenced by anthropogenic nutrients inputs  
686 at the surface, the model realistically simulates the seasonal cycle of chlorophyll. While  
687 ammonium does not exceed typical "natural" values of  $\sim 1 \text{ mmol m}^{-3}$  below the surface,  
688 chlorophyll concentrations regularly reach more than  $2 \text{ mg m}^{-3}$  between 20 and 40 m in  
689 summer, in agreement with *in situ* measurement (Teel et al., 2018; Beman et al., 2011).  
690 (Additional figures to support the analysis are reported in the Supporting Information, Fig.  
691 S23.)

692 However, in regions more heavily influenced by anthropogenic nutrients, such as the  
693 Santa Monica Bay, the chlorophyll maximum progressively deepens from the surface in  
694 winter to about 25 to 30 m depth in spring and summer, with chlorophyll concentrations  
695 exceeding  $5 \text{ mg Chl m}^{-3}$  (Fig. 13a). This subsurface chlorophyll maximum is maintained  
696 for four to five months (Fig. 13b) before the stratification is weakened by winter mixing.

#### 697 4.4.3 Primary production

698 Validation of the rates of primary production, phytoplankton growth and zooplankton  
699 grazing (Table 5) provides an independent check on mechanisms responsible for chloro-  
700 phyll as a state variable. The spatial and temporal frequency of these data, garnered from  
701 CalCOFI observations and literature values, is low. The most data as well as the most  
702 standardized methodologies are available for primary production. However, many of the  
703 primary production measurements used in this validation do not temporally coincide with  
704 the model period. Despite these uncertainties, the model generally reproduces expected  
705 large-scale patterns and seasonal variability in primary production.

706 This large scale variability was also mentioned in Deutsch et al. (2021). Model and data  
707 both show lower productivity in winter (Fig. 14a,c) and higher in spring (Fig. 14b,d), when  
708 the primary production is high along the coastal band, in the northern Bight around the  
709 Channel Islands (Fig. 14d), consistent with observations (Fig. 14b). This is also consistent  
710 with the so-called "green ribbon" of high-chlorophyll observed along the coast throughout  
711 the SCB (Lucas et al., 2011). The model reasonably reproduces the seasonal cycle of primary  
712 production in each of the subregions.



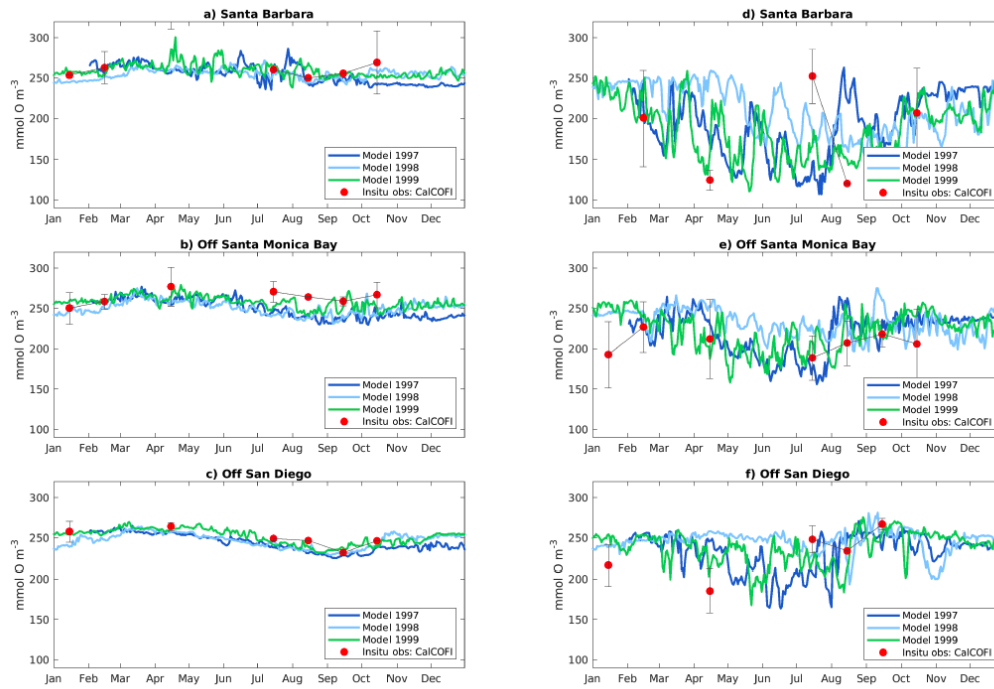


Figure 14: (a)-(b) Maps of vertically integrated Vertically Generalized Production Model (VGPM) net primary production and CalCOFI *in situ* measurements plotted as dots for (a) winter (January and February) and (b) spring (April to June). (c)-(d) Maps of vertically integrated primary production from the model, in (c) winter and (d) spring. Note the higher values for CalCOFI *in situ* measurements as compared to the satellite estimate, in better agreement with the model.

713 Phytoplankton are generally limited by a combination of nutrients and light, the latter  
714 of which is only limiting at depth in the SCB (Deutsch et al., 2021).

715 In winter, nitrogen is high at the surface in the northern SCB, and thus is not limiting.  
716 In the southern SCB, light and nitrogen are co-limiting due to stronger stratification, leading  
717 to oligotrophic conditions. In spring and through the summer, nitrogen is limiting nearly  
718 everywhere except in the Santa Barbara Channel and near the Channel Islands, where  
719 upwelling and submesoscale eddies maintain high nutrients at the surface.

720 The scatter plots in Fig. 14e-f show a comparison of the simulated primary produc-  
721 tion between the *in situ* CalCOFI data and that derived from remote sensing (empirically  
722 adjusting the Behrenfeld&Falkowski Vertically Generalized Production Model [VGPM]).  
723 The model shows a correlation coefficient of about 0.6 with CalCOFI, similarly to that  
724 reported by Kahru et al. (2009) when comparing the VGPM product with CalCOFI. The  
725 model shows a stronger correlation with VGPM data, with a correlation coefficient of the  
726 order of 0.8.

727 Finally, while slightly outside our model domain and simulation period, the modeled  
728 phytoplankton growth and zooplankton grazing rates were within the same order of mag-  
729 nitude as the measured rates from the California Current Long Term Ecological Research  
730 project (CC-LTER, see Landry et al. (2009), and Table 5) in the northern portion of the  
731 Bight.

|   | Bight 13     | Literature | Model       |
|---|--------------|------------|-------------|
| Primary production ( $\text{g C m}^{-2} \text{y}^{-1}$ )                  | 47.4, 1037.4 |            | 250, 1660   |
| Nitrification ( $\text{mmol m}^{-3} \text{d}^{-1}$ )                      | 0, 0.225     | 0.02, 0.08 | 0.001, 0.27 |
| $\text{NO}_3^-$ Uptake Rate ( $\text{mmol N mg Chl}^{-1} \text{d}^{-1}$ ) | 0.005, 2.16  |            | 0.03, 0.15  |
| $\text{NH}_4^+$ Uptake Rate ( $\text{mmol N mg Chl}^{-1} \text{d}^{-1}$ ) | 0.10, 8.30   |            | 0.08, 0.15  |
| Total Phytoplankton Growth $\mu$ ( $\text{d}^{-1}$ )                      |              | 0.05, 0.8  | 0.3, 0.4    |
| Grazing ( $\text{d}^{-1}$ )   |              | 0.02, 0.5  | 0.3, 1.5    |

Table 5: Comparison of biogeochemical rates between published literature and model. Values are minimum and maximum. Literature values come from Landry et al. (2009); Li et al. (2011). Bight 13 is extracted from (McLaughlin et al., 2021) study.

#### 732 4.5 Carbonate system and oxygen parameters

733 The model predicts changes in dissolved oxygen and carbon system parameters related  
734 to photosynthesis and respiration, as well as horizontal transport and vertical mixing. As  
735 described in section 4.4.1, the coasts of Los Angeles and Santa Barbara are hot-spots of  
736 intensified plankton activity, and both systems are impacted by high variability and small-  
737 scale eddy circulation. In the upper layers, photosynthesis increases both dissolved oxygen  
738 and pH (Figs. 16, ??, and 18), consistent with observations in these regions. The Santa  
739 Monica Bay shows the highest oxygen production rates ( $60 \text{ mmol m}^{-2} \text{d}^{-1}$ ), followed by  
740 the Santa Barbara coast ( $57 \text{ mmol m}^{-2} \text{d}^{-1}$ ), while rates in the Orange County and San  
741 Diego coasts are nearly two times lower. Oxygen and carbon are further replenished at the  
742 surface by air-sea gas exchange with the atmosphere. Export of newly-fixed organic carbon  
743 leads in both regions to high remineralization rates that consume oxygen and release carbon  
744 dioxide at depth. We simulate similar high organic matter export (around  $30 \text{ mmol m}^{-2}$   
745  $\text{d}^{-1}$ ) in the Santa Barbara and Los Angeles coasts (see Supporting Information: Fig. S24).

746 The reliability of these predictions can be tested by validation of dissolved oxygen and  
747 carbonate system parameters. There are several sources of uncertainty in the dissolved  
748 oxygen, pH, and aragonite saturation state observational records, which affect data-model  
749 comparisons. For dissolved oxygen, sensors are relatively accurate and precise and have a  
750 rapid response time ( $< 1s$ ) when generating vertically resolved profiles. Repeated field mea-  
751 surement accuracy for CTD dissolved oxygen sensors was reported to be approximately 8  
752  $\text{mmol m}^{-3}$  (Coppola et al., 2013). The pH observational record is particularly fraught with  
753 uncertainty. An evaluation of pH sensor data in the SCB indicated that, while sensor pH  
754 measurements were well correlated with discrete bottle samples collected at the same depth,  
755 there was a clear bias in pH, with sensor measurements under-predicting bottle measure-  
756 ments and high variability in the differences between paired bottle and sensor measurements  
757 ( $\Delta\text{pH}$  ranging from  $\pm 0.5$ ) (McLaughlin, Dickson, et al., 2017). The aragonite saturation  
758 state is estimated using an algorithm developed for the region (Alin et al., 2012) for both  
759 *in situ* observations and model output, because complete measurements of carbon system  
760 parameters required to calculate  $\Omega_{Ar}$  are missing. For all three variables, spatial and tem-  
761 poral under-sampling, particularly during seasons with high variability, adds uncertainty to  
762 the data-model comparison.

#### 763 4.5.1 Vertical gradients and seasonal variability of dissolved oxygen

764 The model reproduces observed seasonal and spatial patterns in dissolved oxygen con-  
765 centration (Fig. 15), accurately simulating magnitude, vertical and horizontal gradients,  
766 and variability. Quantitative statistical analysis (see Table 6) indicated that the model per-  
767 formance was *excellent* or *'good'* for nearly all metrics for all regions and seasons. The lowest  
768 performance of the model was characterized as *poor* for two sub-regions for the Nash-Sutcliff  
769 Model Efficiency during Spring, and *'reasonable'* for some metrics in some sub-regions, which  
770 may be related to under-sampling during seasons with high variability, as described above.  
771 Similar to temperature, we tested whether the variability in spring may be impacting the  
772 performance statistics by extracting random profiles for the region (not shown, expressed  
773 with large error-bars in the spring season plots in Fig. 16), which show how dissolved oxy-  
774 gen on a single arbitrary day can more closely align with the observations. This supports  
775 the hypothesis that observational uncertainty is behind the lack of observational agreement  
776 with the model. Model performance was lowest in the Orange County and San Diego subre-  
777 gions, where model predictions tended to overestimate dissolved oxygen, consistent with the  
778 chlorophyll under-prediction, a likely consequence of the lack of cross-border inputs from  
779 Mexican waters.

780 The model also reproduces the seasonality in dissolved oxygen in all subregions (Fig.  
781 16), characterized by large meridional and vertical variability. Near the Channel Islands,  
782 dissolved oxygen varies at 50 m by up to  $140 \text{ mmol O}_2 \text{ m}^{-3}$  between the highest winter  
783 values and the lowest summer values, reflecting the dynamics of upwelling, productivity, and  
784 air-sea gas-exchange. Offshore the coasts of Santa Monica and San Diego, the variability  
785 between winter and summer is of the order of  $80\text{-}90 \text{ mmol O}_2 \text{ m}^{-3}$ . Surface concentrations  
786 are everywhere above  $240 \text{ mmol O}_2 \text{ m}^{-3}$  year-round, consistent with observations. The  
787 highest summer concentrations are observed at the depth of the deep chlorophyll maximum,  
788 reflecting photosynthesis, while decreasing at depth to below  $150 \text{ mmol O}_2 \text{ m}^{-3}$ . These  
789 patterns are generally consistent with observations in the same regions.

790 During the 1998 El Niño event, the model shows a net decrease of dissolved oxygen  
791 near the surface, and a net increase below it. During this period, the entire upper layer (0-80  
792 m) is characterized by a homogeneous oxygen concentration of about  $240 \text{ mmol O}_2 \text{ m}^{-3}$   
793 over almost the entire SCB (not shown). Only the San Pedro and Santa Monica Bays show  
794 higher concentrations, which we attribute to the local anthropogenic nutrient enrichment  
795 and subsequent blooms (see Fig. 19). This is consistent with observations of the 1998 El  
796 Niño event in California coastal waters (Chavez et al., 2002; Booth et al., 2014).

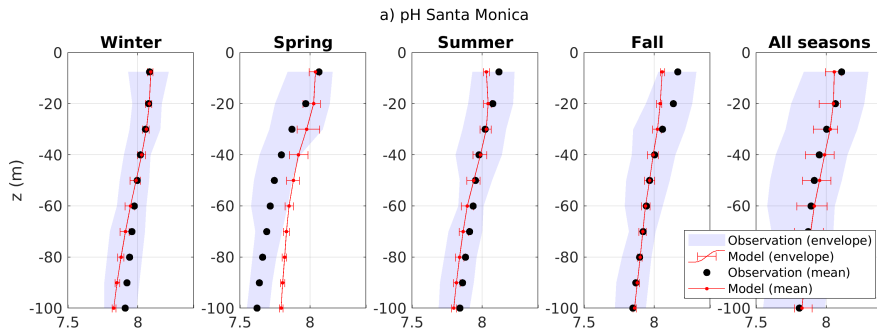


Figure 15: As for Fig. 5, but for oxygen concentration.

| Santa Monica |     |                         |         |               |             |                              |                                 |                        |
|--------------|-----|-------------------------|---------|---------------|-------------|------------------------------|---------------------------------|------------------------|
|              | H   | Correlation Coefficient | p-value | Cost Function | Oxygen Bias | Ratio of Standard Deviations | Nash-Sutcliffe Model Efficiency | Number of observations |
| Winter       | 0 E | 0.97 E                  | 9E-07 E | 0.14 E        | -0.09 E     | 1.20 G                       | 0.77 E                          | 716                    |
| Spring       | 0 E | 0.91 E                  | 3E-04 E | 0.26 E        | -0.23 R     | 1.03 E                       | 0.37 R                          | 702                    |
| Summer       | 0 E | 0.99 E                  | 2E-10 E | 0.07 E        | 0.07 E      | 0.99 E                       | 0.86 E                          | 712                    |
| Fall         | 0 E | 0.97 E                  | 2E-06 E | 0.19 E        | -0.14 G     | 1.49 P                       | 0.42 R                          | 718                    |
| All Seasons  | 0 E | 0.97 E                  | 3E-06 E | 0.14 E        | -0.11 G     | 1.18 G                       | 0.69 E                          | 2848                   |
| pH           |     |                         |         |               |             |                              |                                 |                        |
|              | H   | Correlation Coefficient | p-value | Cost Function | Bias        | Ratio of Standard Deviations | Nash-Sutcliffe Model Efficiency | Number of observations |
| Winter       | 0 E | 0.99 E                  | 2E-08 E | 0.01 E        | 0.01 E      | 0.59 P                       | 0.57 G                          | 632                    |
| Spring       | 0 E | 0.97 E                  | 2E-06 E | 0.02 E        | -0.02 E     | 1.45 P                       | 0.15 P                          | 702                    |
| Summer       | 0 E | 0.96 E                  | 9E-06 E | 0.01 E        | 0.01 E      | 1.01 E                       | 0.85 E                          | 712                    |
| Fall         | 0 E | 0.97 E                  | 3E-06 E | 0.01 E        | 0.01 E      | 1.49 P                       | 0.78 E                          | 715                    |
| All Seasons  | 0 E | 0.97 E                  | 5E-06 E | 0.01 E        | -0.01 E     | 1.12 G                       | 0.84 E                          | 2761                   |

Table 6: Statistical comparison between *in situ* data and model outputs for dissolved oxygen and pH profile in Santa Monica Bay.

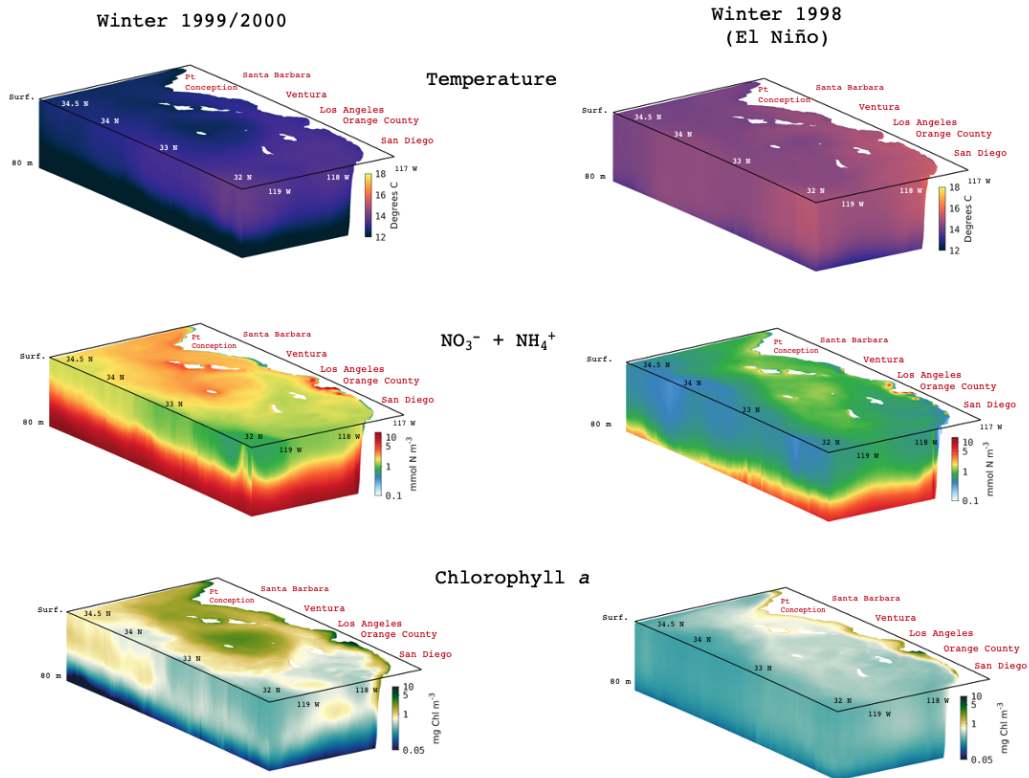


Figure 16: Comparison of dissolved oxygen concentration between different years of model output, and a climatology from CalCOFI *in situ* data. SB is near the center of Santa Barbara Channel, SM is offshore the Santa Monica Bay, and SD is offshore San Diego. Left panels show surface concentrations, right panels concentrations at 50 m depth.



797  
798

## 4.5.2 Vertical gradients and seasonal variability of carbon system parameters

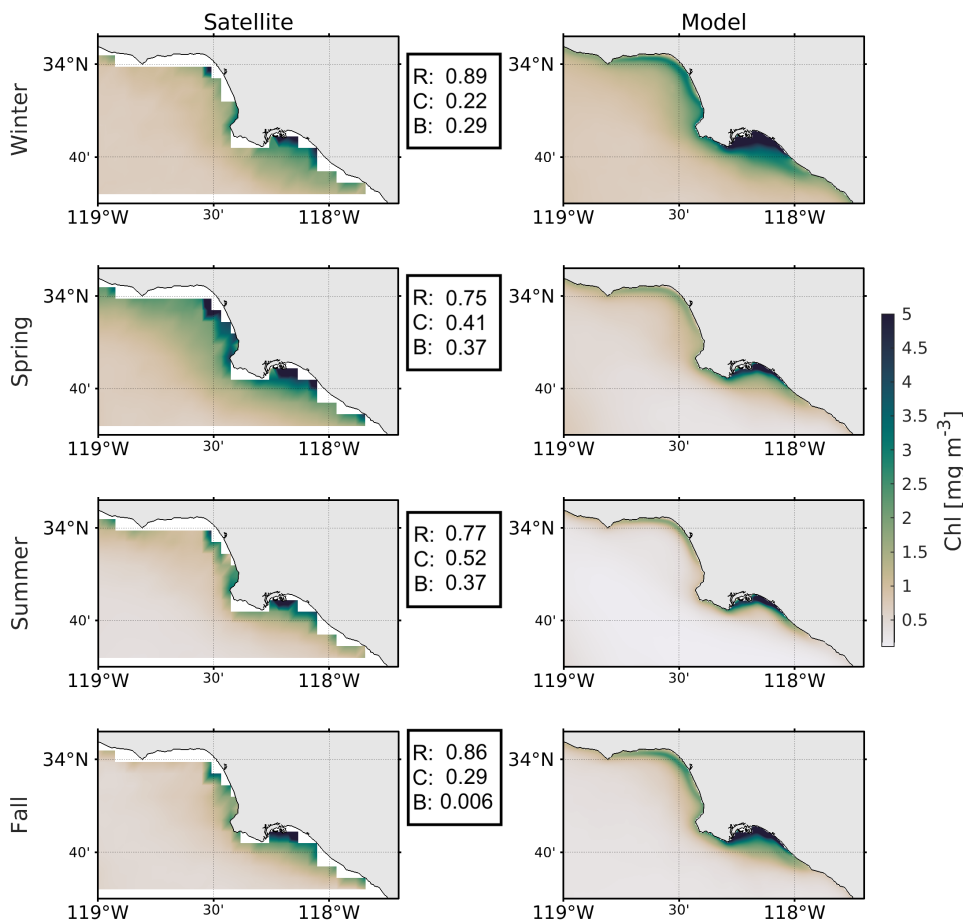


Figure 17: As for Fig. 5 but for seawater pH.

799  
800  
801  
802  
803  
804  
805  
806  
807  
808  
809  
810  
811  
812

Together with pH, the saturation state of aragonite ( $\Omega_{Ar}$ ) is often used as a metric to identify the potential impact of Ocean Acidification on marine calcifiers, because it is a measure of the availability of carbonate ions for calcium carbonate precipitation (Bednarsek et al., 2019).  $\Omega_{Ar}$  shows similar vertical variability as dissolved oxygen (Juraneck et al., 2009; Alin et al., 2012). Similar to oxygen loss, reduction in pH and  $\Omega_{Ar}$  in the upper layers can be caused by coastal upwelling and local physical processes (Feely et al., 2018); over longer timescales it also reflects oceanic uptake of anthropogenic carbon from the atmosphere. We utilize sensor pH data sets to evaluate vertical profiles in the carbonate system. Because of the known uncertainty in pH measurements, we are most concerned with how well the model reproduced the shape of the profiles (i.e., goodness of fit estimates, as with chlorophyll). Sensor-derived pH profile measurements should be internally consistent within a data set (if the sensor is working properly and if pressure issues are minimal), providing some value to goodness of fit assessments. Given these constraints, the data-model comparisons for pH sensor data were generally *excellent* or *good* for all sub-regions

813 and all seasons 17. Unsurprisingly, the model performance reproducing observational means  
 814 and variability was generally *reasonable* or *poor* for most sub-regions and seasons, with some,  
 815 if not most, of this disagreement due to difficulties in conducting a validation of the model  
 816 with large uncertainties in sensor-derived pH profiles. Recently, the CalCOFI program has  
 817 incorporated  $\Omega_{Ar}$  into its sampling design. Although the data do not line up with the  
 818 model period, they are useful for evaluating seasonal variability in the model. Generally,  
 819 the model reproduces seasonal and vertical variability in  $\Omega_{Ar}$ , with higher saturation states  
 820 in the summer and fall, when waters are generally more stratified, and lower values in  
 821 winter and spring, when upwelling brings undersaturated waters closer to the surface.  $\Omega_{Ar}$   
 822 is also much lower and more highly variable at depth. These patterns are consistent with  
 823 observations throughout the SCB (McLaughlin et al., 2018).

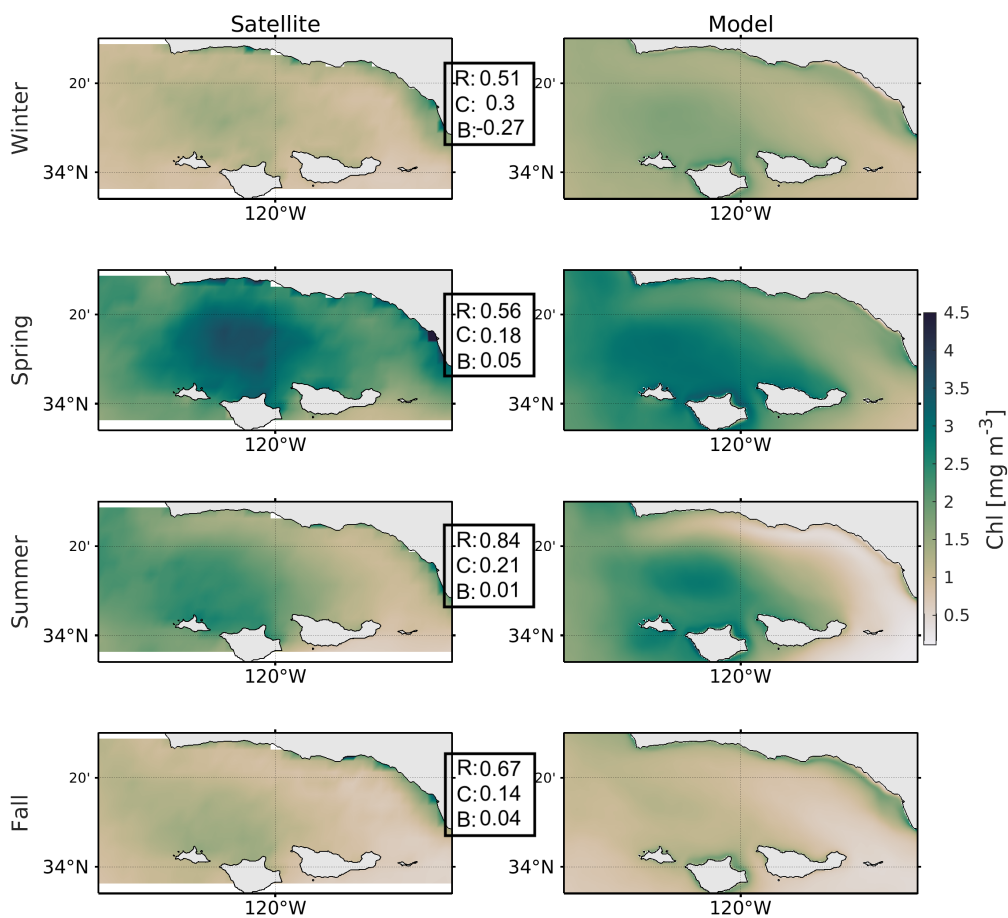


Figure 18: Comparison of the saturation state of aragonite between different years of model output, and a climatology from CalCOFI *in situ* data. SB is near the center of Santa Barbara Channel, SM is offshore the Santa Monica Bay, and SD is offshore San Diego. Left panels show surface values, right panels values at 50 m depth.

## 5 Discussion and conclusions

In this study, we demonstrated the readiness of a high-resolution, dynamically down-scaled, physical-biogeochemical model to mechanistically investigate links between a comprehensive reconstruction of terrestrial and atmospheric nutrient inputs, coastal eutrophication, and biogeochemical change in the SCB coastal waters. This modeling platform is an important achievement because it strikes a balance of capturing the forcing of coast-wide basin mesoscale phenomena, while capturing the combined effects of bathymetry and sub-mesoscale eddies that intensify transport of nutrients and biological material. Moreover, this model allows hindcast simulations of primary production, ocean acidification and oxygen loss at timescales that can approach the multi-annual frequencies of intrinsic ocean variability. Future research using this model will make the grand challenge of disentangling natural variability, climate change, and local anthropogenic forcing a tractable task in the near-term. The model evaluation developed in this manuscript discusses sources of uncertainties for the circulation, nitrogen, carbon and oxygen cycles that serve as a critical element to communicate results to regional stakeholders.

ROMS has a long history of validation and management acceptance through various applications in the CCS (e.g. Marchesiello et al. (2003); Capet et al. (2004); Capet, Colas, et al. (2008); Capet, Campos, and Paiva (2008); Capet, McWilliams, et al. (2008); Shchepetkin and McWilliams (2011); Renault, Molemaker, Gula, et al. (2016)). In contrast, experience with BEC within the SCB is more limited. Our validation study of coastal eutrophication gradients in the SCB nearshore complements the U.S. West Coast-wide study of (Deutsch et al., 2021) and strengthens confidence that the basic CCS BEC model formulation, forcing and parameterization is appropriate not only for coastwide analyses, but also for detailed local studies of coastal eutrophication in the highly urbanized SCB (Kessouri et al., 2021).

In Table 1, we summarize a series of statistical tests of model performance, and provide guidelines for their interpretation. These tests are helpful for the validation and interpretation of the model results, because they quantify in an accessible and succinct way information related to magnitude, variability, gradients, and systematic biases of model variables relative to observations. We further apply these tests to the most relevant biogeochemical variables (see Tables 2, 3, 4 and 6). In particular, tests that compare variability are essential for a model that resolves submesoscale circulation and the environmental heterogeneity it produces. These tests are used to build confidence in the use of the model for coastal applications, including scenarios and attribution experiments (Kessouri et al., 2021). Likewise, they could be helpful metrics for multi-model ensemble comparisons.

The representation of physical processes such as vertical mixing and horizontal circulation was consistent across the model and measurements. The model reproduces the main structure of the climatological upwelling front and cross-shore isopycnal slopes, and the mean current patterns and associated temperature gradients. We also demonstrate good agreement between model simulations and the mean distributions and variability of key ecosystem metrics, including surface nutrients and productivity, and subsurface  $O_2$  and carbonate saturation. The spatial patterns of primary production, phytoplankton growth rates, and zooplankton grazing are broadly consistent with measured rates. The distribution of primary production is governed by the trade-off between nutrient and light limitation, a balance that reproduces and explains the observed spatial variations in the depth of the deep chlorophyll maximum. Statistical measures of model agreement on biogeochemical state variables was excellent to good and the range of predicted biogeochemical rates on par with observations. Under the realistic flow fields produced by ROMS, the conformity of model predictions with a rich observational dataset is a strong demonstration of model validity for coastal eutrophication applications (Kessouri et al., 2021). We also demonstrated that the model responds with confidence to the variability caused by El Niño, modifying the vertical distribution of the physical and biogeochemical properties across the upper ocean of the entire Bight, as illustrated by the three-dimensional change in key ocean variables shown in Fig. 19.

877 While the broad agreement between the model and observations for a range of variables  
878 is encouraging, some aspects of the model require further investigation and improvement.  
879 Some of the model biases are shared across multiple variables, reflecting common underlying  
880 processes, such as stoichiometry of biogeochemical reactions and solubility. We highlighted  
881 some of these biases, for example: (1) Spring is the season when we see the largest variability,  
882 in particular between March and June, when we move from vigorous surface mixing to  
883 a strong stratification; (2) Along the coasts of Orange County and San Diego, missing  
884 nutrients sources from the southern boundary (i.e., from the Mexican coast) likely drive  
885 underestimation of phytoplankton concentration, productivity, and carbon export, causing  
886 an overestimation of oxygen, pH and calcium carbonate saturation in the subsurface; (3)  
887 Overestimation of temperature in the water column impacts oxygen and carbon solubility  
888 by decreasing their equilibrium concentrations; this suggests that some biases, such as too  
889 high oxygen in spring, hide overcompensation by other biogeochemical processes, e.g. high  
890 productivity or reduced gas exchange; (4) Underestimation or overestimation of pH and  
891 calcium carbonate saturation state are tightly linked by inorganic carbon chemistry, and  
892 can in turn reflect biases in circulation, water column structure, temperature, and nutrient  
893 cycles of the type discussed above.

894 The structure of the model is also limited in its representation of ecosystem dynamics.  
895 For example, phytoplankton diversity is limited in the model, preventing it from properly  
896 simulating events such as dinoflagellate-driven red tides, which occur over short periods on  
897 nearshore coastal scales, typically in spring. Despite the good performance of the model  
898 in reproducing total primary production and grazing rates, the model does not include  
899 multiple zooplankton functional groups, thus providing little information on the dynamics  
900 and transfer of energy to higher trophic levels, or the formation of rapidly sinking fecal  
901 pellets. From a hydrodynamics point of view, with a horizontal resolution of 300m, the model  
902 does not directly resolve physical processes occurring at scales of tens of meters (Dauhajre et  
903 al., 2019), for example the dilution and entrainment of buoyant wastewater plumes, which  
904 are parameterized in the model, or the vertical and horizontal transport of tracers in the  
905 very nearshore surf zone.

906 Quantitative and qualitative results of confidence assessments are essential for informing  
907 management decisions, evaluating management strategies, and providing a basis for risk  
908 analyses. The most successful management approaches are those that explicitly incorporate  
909 uncertainty (e.g. Taylor et al. (2000)). An assessment of model validation must consider  
910 the complex combination of model and observational uncertainties (Allen et al., 2007),  
911 including: 1) uncertainty/error in the model, with the inclusion of intrinsic variability; 2)  
912 uncertainty/error in measured data; 3) uncertainty from the difference in spatial scale of the  
913 model output relative to the measured data used in the comparison (specifically, comparing  
914 a 0.3 km grid cell to a discrete sampling station); and 4) uncertainty from the difference in  
915 temporal averaging of the model output relative to the measured data. For parameters in  
916 which we have high confidence in the observational record, i.e., temperature and dissolved  
917 oxygen, model performance statistics show excellent agreement for mean profiles, vertical  
918 and horizontal gradients, as well as seasonal variability. The model reproduces chlorophyll  
919 reasonably well, albeit with some biases, which can be in part attributed to a simplified  
920 representation of plankton diversity, measurement uncertainty, sparseness of *in situ* data,  
921 cloud cover and algorithm biases in satellite products. Variables such as pH and ammonium  
922 show lower agreement, likely due to measurement uncertainty and sampling bias, but general  
923 spatial and temporal patterns are correctly reproduced in the model.

924 Greater clarity is needed in the requirements for model performance and uncertainty to  
925 support decisions on management of SCB coastal water quality and eutrophication (Boesch,  
926 2019). These requirements are likely to be driven largely by the approach that will be used  
927 to interpret a "significant impact" (e.g. existing water quality pH and dissolved oxygen cri-  
928 teria, or biologically relevant thresholds; (Weisberg et al., 2016)), as these have significant  
929 implications for required model precision and accuracy on different spatial and and temporal

930 scales. Future efforts to constrain uncertainty could include sensitivity analyses and model  
 931 ensemble comparisons of the BEC biogeochemical component with other biogeochemical  
 932 models that feature increasingly complex representations of planktonic functional groups,  
 933 benthic communities, and sediment-pelagic interactions. Finally, long-term investments are  
 934 needed in coupled chemical-biological observations of phytoplankton and zooplankton di-  
 935 versity and community structure. These observations are critical to provide understanding  
 936 of the evolution of lower trophic ecosystem structure with climate change, and their rela-  
 937 tionship with biogeochemical cycles linked to ocean acidification and oxygen loss (Sailley et  
 938 al., 2013). Ultimately, the need to constrain uncertainty will likely scale with the economic  
 939 import of management decisions under consideration, which could range from increased  
 940 monitoring requirements to multi-billion dollar non-point source controls and wastewater  
 941 treatment plant upgrades.

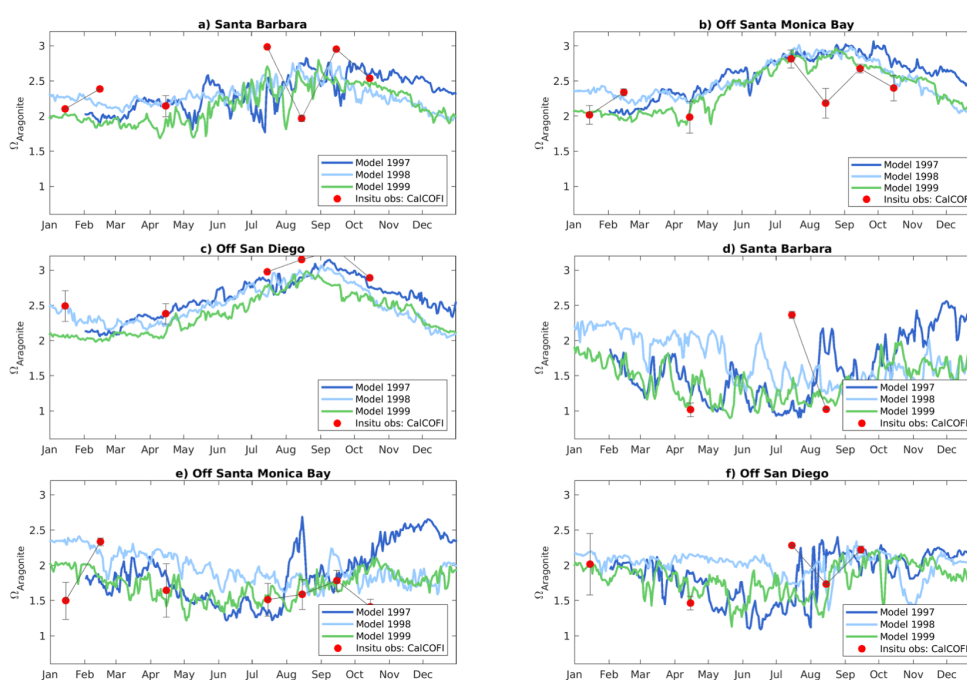


Figure 19: Three-dimensional illustration of temperature, DIN ( $\text{NO}_3^- + \text{NH}_4^+$ ) and chlorophyll in the Southern California Bight. Panels show winter 1999 and 2000 (left panels), winter 1998 during El Niño period (right panels).

## Acknowledgments

942 This research was supported by the National Oceanic and Atmospheric Administration under  
 943 grants for ocean acidification NA15NOS4780186 and marine debris NA19NOS9990086,  
 944 California Ocean Protection Council grant C0100400, and NSF grants OCE-1419323 and  
 945 OCE-1419450. This work was supported by National Oceanic and Atmospheric Admin-  
 946 istration under ECOHAB award NA18NOS4780174. This is ECOHAB publication 980.  
 947 Computational resources were provided by the Extreme Science and Engineering Discovery  
 948 Environment (XSEDE) through allocation TG-OCE170017, and by the super-computer  
 949 Hoffman2 at the University of California Los Angeles, at the Institute for Digital Research  
 950 and Education (IDRE, UCLA). Code is available in (Kessouri, McWilliams, et al., 2020).  
 951 In situ observation data to generate the figures and statistics are available in (Kessouri,  
 952 McLaughlin, et al., 2020). Local land-based and atmospheric data can be found in (Sutula



954 et al., 2021a). I wish to extend my special thanks to the three anonymous reviewers for  
 955 helping improving this manuscript.

## 956 References

- 957 Alin, S. R., Feely, R. A., Dickson, A. G., Hernández-Ayón, J. M., Juranek, L. W., Ohman,  
 958 M. D., & Goericke, R. (2012). Robust empirical relationships for estimating the  
 959 carbonate system in the southern california current system and application to calcofi  
 960 hydrographic cruise data (2005–2011). *Journal of Geophysical Research: Oceans*,  
 961 *117*(C5).
- 962 Allen, J., Somerfield, P., & Gilbert, F. (2007). Quantifying uncertainty in high-resolution  
 963 coupled hydrodynamic-ecosystem models. *Journal of Marine Systems*, *64*(1-4), 3–14.
- 964 Arhonditsis, G., Tsirtsis, G., Angelidis, M., & Karydis, M. (2000). Quantification of the  
 965 effects of nonpoint nutrient sources to coastal marine eutrophication: applications to a  
 966 semi-enclosed gulf in the mediterranean sea. *Ecological Modelling*, *129*(2-3), 209–227.
- 967 Armstrong, R. A., Lee, C., Hedges, J. I., Honjo, S., & Wakeham, S. G. (2001). A new,  
 968 mechanistic model for organic carbon fluxes in the ocean based on the quantitative  
 969 association of poc with ballast minerals. *Deep Sea Research Part II: Topical Studies*  
 970 *in Oceanography*, *49*(1-3), 219–236.
- 971 Bednarsek, N., Feely, R. A., Howes, E. L., Hunt, B., Kessouri, F., León, P., ... others  
 972 (2019). Systematic review and meta-analysis towards synthesis of thresholds of ocean  
 973 acidification impacts on calcifying pteropods and interactions with warming. *Frontiers*  
 974 *in Marine Science*, *6*, 227.
- 975 Behrenfeld, M. J., & Falkowski, P. G. (1997). Photosynthetic rates derived from  
 976 satellite-based chlorophyll concentration. *Limnology and Oceanography*, *42*(1), 1-20.  
 977 Retrieved from [https://aslopubs.onlinelibrary.wiley.com/doi/abs/10.4319/](https://aslopubs.onlinelibrary.wiley.com/doi/abs/10.4319/10.1997.42.1.0001)  
 978 [10.1997.42.1.0001](https://doi.org/10.4319/10.1997.42.1.0001) doi: <https://doi.org/10.4319/10.1997.42.1.0001>
- 979 Beman, J. M., Steele, J. A., & Fuhrman, J. A. (2011). Co-occurrence patterns for abundant  
 980 marine archaeal and bacterial lineages in the deep chlorophyll maximum of coastal  
 981 california. *The ISME journal*, *5*(7), 1077–1085.
- 982 Boesch, D. F. (2019). Barriers and bridges in abating coastal eutrophication. *Frontiers in*  
 983 *Marine Science*, *6*, 123.
- 984 Boesch, D. F., Brinsfield, R. B., & Magnien, R. E. (2001). Chesapeake bay eutrophication:  
 985 Scientific understanding, ecosystem restoration, and challenges for agriculture. *Journal*  
 986 *of Environmental Quality*, *30*(2), 303–320.
- 987 Bograd, S. J., Buil, M. P., Di Lorenzo, E., Castro, C. G., Schroeder, I. D., Goericke, R.,  
 988 ... Whitney, F. A. (2015). Changes in source waters to the southern california bight.  
 989 *Deep Sea Research Part II: Topical Studies in Oceanography*, *112*, 42–52.
- 990 Booth, J., Woodson, C., Sutula, M., Micheli, F., Weisberg, S., Bograd, S., ... Crowder, L.  
 991 (2014). Patterns and potential drivers of declining oxygen content along the southern  
 992 california coast. *Limnology and Oceanography*, *59*(4), 1127–1138.
- 993 Brzezinski, M. A., & Washburn, L. (2011). Phytoplankton primary productivity in the santa  
 994 barbara channel: Effects of wind-driven upwelling and mesoscale eddies. *Journal of*  
 995 *Geophysical Research: Oceans*, *116*(C12).
- 996 Byun, D. W., Song, C.-K., Percell, P., Pleim, J., Otte, T., Young, J., & Mathur, R. (2006).  
 997 Linkage between wrf/nmm and cmaq models. In *Presentation at 5th annual cmas*  
 998 *conference, chapel hill, nc, available at: www.cmascenter.org* (pp. 16–18).
- 999 Capet, X., Campos, E., & Paiva, A. (2008). Submesoscale activity over the Argentinian  
 1000 shelf. *Geophysical Research Letters*, *35*(15).
- 1001 Capet, X., Colas, F., McWilliams, J. C., Penven, P., & Marchesiello, P. (2008). Eddies  
 1002 in eastern boundary subtropical upwelling systems. *Ocean Modeling in an Eddying*  
 1003 *Regime, Geophys. Monogr. Ser.*, *177*, 131–147.
- 1004 Capet, X., Klein, P., Hua, B. L., Lapeyre, G., & McWilliams, J. C. (2008). Surface kinetic  
 1005 energy transfer in surface quasi-geostrophic flows. *Journal of Fluid Mechanics*, *604*,  
 1006 165–174.

- 1007 Capet, X., Marchesiello, P., & McWilliams, J. (2004). Upwelling response to coastal wind  
1008 profiles. *Geophysical Research Letters*, *31*(13).
- 1009 Capet, X., McWilliams, J. C., Molemaker, M. J., & Shchepetkin, A. (2008). Mesoscale  
1010 to submesoscale transition in the California Current System. Part I: Flow structure,  
1011 eddy flux, and observational tests. *Journal of Physical Oceanography*, *38*(1), 29–43.
- 1012 Cederwall, H., & Elmgren, R. (1990). Biological effects of eutrophication in the baltic sea,  
1013 particularly the coastal zone. *Ambio. Stockholm*, *19*(3), 109–112.
- 1014 Cerco, C. F., & Cole, T. (1993). Three-dimensional eutrophication model of chesapeake  
1015 bay. *Journal of Environmental Engineering*, *119*(6), 1006–1025.
- 1016 Chavez, F., Pennington, J., Castro, C., Ryan, J., Michisaki, R., Schlining, B., ... Collins,  
1017 C. (2002). Biological and chemical consequences of the 1997–1998 el niño in central  
1018 california waters. *Progress in Oceanography*, *54*(1-4), 205–232.
- 1019 Coppola, L., Salvetat, F., Delauney, L., BSH, D. M., Karstensen, J., & Thierry, V. (2013).  
1020 White paper on dissolved oxygen measurements: scientific needs and sensors accuracy.  
1021 *Jerico Project*.
- 1022 Cullen, J. (2001). *Primary production methods*. London, UK: Academic Press.
- 1023 Dauhajre, D. P., McWilliams, J. C., & Renault, L. (2019). Nearshore lagrangian con-  
1024 nectivity: Submesoscale influence and resolution sensitivity. *Journal of Geophysical  
1025 Research: Oceans*, *124*(7), 5180–5204.
- 1026 de Boyer Montégut, C., Madec, G., Fischer, A. S., Lazar, A., & Iudicone, D. (2004). Mixed  
1027 layer depth over the global ocean: An examination of profile data and a profile-based  
1028 climatology. *Journal of Geophysical Research: Oceans*, *109*(C12).
- 1029 Derrick, B., Toher, D., & White, P. (2016). Why Welch’s test is Type I error robust.  
1030 *QUANTITATIVE METHODS FOR PSYCHOLOGY*, *12*(1), 30-38. doi: {10.20982/  
1031 tqmp.12.1.p030}
- 1032 Deutsch, C., Frenzel, H., McWilliams, J. C., Renault, L., Kessouri, F., Howard, E., ...  
1033 Yang, S. (2021). Biogeochemical variability in the california current system. *Progress  
1034 in Oceanography*, 102565.
- 1035 DiGiacomo, P. M., Washburn, L., Holt, B., & Jones, B. H. (2004). Coastal pollution  
1036 hazards in southern california observed by sar imagery: stormwater plumes, wastew-  
1037 ater plumes, and natural hydrocarbon seeps. *Marine Pollution Bulletin*, *49*(11-12),  
1038 1013–1024.
- 1039 Dong, C., Idica, E. Y., & McWilliams, J. C. (2009). Circulation and multiple-scale variability  
1040 in the southern california bight. *Progress in Oceanography*, *82*(3), 168–190.
- 1041 Fasham, M. J. (1993). Modelling the marine biota. In *The global carbon cycle* (pp. 457–504).  
1042 Springer.
- 1043 Feely, R. A., Okazaki, R. R., Cai, W.-J., Bednaršek, N., Alin, S. R., Byrne, R. H., &  
1044 Fassbender, A. (2018). The combined effects of acidification and hypoxia on ph and  
1045 aragonite saturation in the coastal waters of the california current ecosystem and the  
1046 northern gulf of mexico. *Continental Shelf Research*, *152*, 50–60.
- 1047 Fennel, K., & Testa, J. M. (2019). Biogeochemical controls on coastal hypoxia. *Annual  
1048 Review of Marine Science*, *11*, 105–130.
- 1049 Galarza, J. A., Carreras-Carbonell, J., Macpherson, E., Pascual, M., Roques, S., Turner,  
1050 G. F., & Rico, C. (2009). The influence of oceanographic fronts and early-life-history  
1051 traits on connectivity among littoral fish species. *Proceedings of the National Academy  
1052 of Sciences*, *106*(5), 1473–1478.
- 1053 Gruber, N. (2004). The dynamics of the marine nitrogen cycle and its influence on atmo-  
1054 spheric co 2 variations. In *The ocean carbon cycle and climate* (pp. 97–148). Springer.
- 1055 Gruber, N., Lachkar, Z., Frenzel, H., Marchesiello, P., Münnich, M., McWilliams, J. C., ...  
1056 Plattner, G.-K. (2011). Eddy-induced reduction of biological production in eastern  
1057 boundary upwelling systems. *Nature geoscience*, *4*(11), 787.
- 1058 Ho, M., Molemaker, J. M., Kessouri, F., McWilliams, J. C., & Gallien, T. W. (2021).  
1059 High-resolution nonhydrostatic outfall plume modeling: Cross-flow validation. *Journal  
1060 of Hydraulic Engineering*, *147*(8), 04021028. Retrieved from [https://ascelibrary  
1061 .org/doi/abs/10.1061/%28ASCE%29HY.1943-7900.0001896](https://ascelibrary.org/doi/abs/10.1061/%28ASCE%29HY.1943-7900.0001896) doi: 10.1061/(ASCE)

- 1062 HY.1943-7900.0001896  
 1063 Howard, M. D., Sutula, M., Caron, D. A., Chao, Y., Farrara, J. D., Frenzel, H., . . . Sengupta,  
 1064 A. (2014). Anthropogenic nutrient sources rival natural sources on small scales in the  
 1065 coastal waters of the southern california bight. *Limnology and Oceanography*, *59*(1),  
 1066 285–297.  
 1067 Juranek, L., Feely, R., Peterson, W., Alin, S., Hales, B., Lee, K., . . . Peterson, J. (2009).  
 1068 A novel method for determination of aragonite saturation state on the continental  
 1069 shelf of central oregon using multi-parameter relationships with hydrographic data.  
 1070 *Geophysical Research Letters*, *36*(24).  
 1071 Justić, D., Rabalais, N. N., & Turner, R. E. (2005). Coupling between climate variability  
 1072 and coastal eutrophication: evidence and outlook for the northern gulf of mexico.  
 1073 *Journal of Sea Research*, *54*(1), 25–35.  
 1074 Kahru, M., Kudela, R., Manzano-Sarabia, M., & Mitchell, B. G. (2009). Trends in primary  
 1075 production in the california current detected with satellite data. *Journal of Geophysical*  
 1076 *Research: Oceans*, *114*(C2).  
 1077 Kang, X., Zhang, R.-H., & Wang, G. (2017). Effects of different freshwater flux repre-  
 1078 sentations in an ocean general circulation model of the tropical pacific. *Science Bul-*  
 1079 *letin*, *62*(5), 345 - 351. Retrieved from [http://www.sciencedirect.com/science/](http://www.sciencedirect.com/science/article/pii/S2095927317300932)  
 1080 [article/pii/S2095927317300932](http://www.sciencedirect.com/science/article/pii/S2095927317300932) doi: <https://doi.org/10.1016/j.scib.2017.02.002>  
 1081 Kessouri, F., Bianchi, D., Renault, L., McWilliams, J. C., Frenzel, H., & Deutsch, C. A.  
 1082 (2020). Submesoscale currents modulate the seasonal cycle of nutrients and pro-  
 1083 ductivity in the california current system. *Global Biogeochemical Cycles*, *34*(10),  
 1084 e2020GB006578.  
 1085 Kessouri, F., McLaughlin, K., Sutula, M., Ho, M., McWilliams, J., C, & Bianchi, D.  
 1086 (2020, August). *Collection of in situ monitoring data in the Southern California*  
 1087 *Bight 1950-2017 for model validation*. Zenodo. Retrieved from [https://doi.org/](https://doi.org/10.5281/zenodo.4536641)  
 1088 [10.5281/zenodo.4536641](https://doi.org/10.5281/zenodo.4536641) doi: [10.5281/zenodo.4536641](https://doi.org/10.5281/zenodo.4536641)  
 1089 Kessouri, F., McWilliams, C. J., Deutsch, C., Renault, L., Frenzel, H., Bianchi, D., &  
 1090 Molemaker, J. (2020, August). *ROMS-BEC oceanic physical and biogeochemical model*  
 1091 *code for the Southern California Current System V2020*. Zenodo. Retrieved from  
 1092 <https://doi.org/10.5281/zenodo.3988618> doi: [10.5281/zenodo.3988618](https://doi.org/10.5281/zenodo.3988618)  
 1093 Kessouri, F., McWilliams, J. C., Bianchi, D., Sutula, M., Renault, L., Deutsch, C., . . .  
 1094 others (2021). Coastal eutrophication drives acidification, oxygen loss, and ecosystem  
 1095 change in a major oceanic upwelling system. *Proceedings of the National Academy of*  
 1096 *Sciences*, *118*(21).  
 1097 Kim, S. Y., Terrill, E. J., Cornuelle, B. D., Jones, B., Washburn, L., Moline, M. A., . . .  
 1098 Kosro, P. M. (2011). Mapping the u.s. west coast surface circulation: A multiyear anal-  
 1099 ysis of high-frequency radar observations. *Journal of Geophysical Research: Oceans*,  
 1100 *116*(C3). Retrieved from [https://agupubs.onlinelibrary.wiley.com/doi/abs/](https://agupubs.onlinelibrary.wiley.com/doi/abs/10.1029/2010JC006669)  
 1101 [10.1029/2010JC006669](https://agupubs.onlinelibrary.wiley.com/doi/abs/10.1029/2010JC006669) doi: <https://doi.org/10.1029/2010JC006669>  
 1102 Kudela, R. M., Howard, M. D., Hayashi, K., & Beck, C. (2017). Evaluation of uptake kinetics  
 1103 during a wastewater diversion into nearshore coastal waters in southern california.  
 1104 *Estuarine, Coastal and Shelf Science*, *186*, 237–249.  
 1105 Landry, M. R., Ohman, M. D., Goericke, R., Stukel, M. R., & Tsyrklevich, K. (2009).  
 1106 Lagrangian studies of phytoplankton growth and grazing relationships in a coastal  
 1107 upwelling ecosystem off southern california. *Progress in Oceanography*, *83*(1-4), 208–  
 1108 216.  
 1109 Large, W. B. (2006). Surface fluxes for practitioners of global ocean data assimilation. In  
 1110 *Ocean weather forecasting* (pp. 229–270). Springer.  
 1111 Large, W. G., McWilliams, J. C., & Doney, S. C. (1994). Oceanic vertical mixing: A review  
 1112 and a model with a nonlocal boundary layer parameterization. *Reviews of Geophysics*,  
 1113 *32*(4), 363–403.  
 1114 Laurent, A., Fennel, K., Ko, D. S., & Lehrter, J. (2018). Climate change projected to  
 1115 exacerbate impacts of coastal eutrophication in the northern gulf of mexico. *Journal*  
 1116 *of Geophysical Research: Oceans*, *123*(5), 3408–3426.

- 1117 Leinweber, A., Gruber, N., Frenzel, H., Friederich, G., & Chavez, F. (2009). Diurnal carbon  
1118 cycling in the surface ocean and lower atmosphere of santa monica bay, california.  
1119 *Geophysical research letters*, *36*(8).
- 1120 Lévy, M., Ferrari, R., Franks, P. J., Martin, A. P., & Rivière, P. (2012). Bringing physics  
1121 to life at the submesoscale. *Geophysical Research Letters*, *39*(14).
- 1122 Li, Q. P., Franks, P. J., & Landry, M. R. (2011). Microzooplankton grazing dynamics: pa-  
1123 rameterizing grazing models with dilution experiment data from the california current  
1124 ecosystem. *Marine Ecology Progress Series*, *438*, 59–69.
- 1125 Lucas, A. J., Dupont, C. L., Tai, V., Largier, J. L., Palenik, B., & Franks, P. J. (2011). The  
1126 green ribbon: Multiscale physical control of phytoplankton productivity and commu-  
1127 nity structure over a narrow continental shelf. *Limnology and Oceanography*, *56*(2),  
1128 611–626.
- 1129 Lyon, G. S., & Stein, E. D. (2009). How effective has the clean water act been at reducing  
1130 pollutant mass emissions to the southern california bight over the past 35 years?  
1131 *Environmental monitoring and assessment*, *154*(1-4), 413.
- 1132 Mahadevan, A. (2016). The impact of submesoscale physics on primary productivity of  
1133 plankton. *Annual Review of Marine Science*, *8*, 161–184.
- 1134 Mahowald, N. M., Yoshioka, M., Collins, W. D., Conley, A. J., Fillmore, D. W., & Coleman,  
1135 D. B. (2006). Climate response and radiative forcing from mineral aerosols during the  
1136 last glacial maximum, pre-industrial, current and doubled-carbon dioxide climates.  
1137 *Geophysical Research Letters*, *33*(20).
- 1138 Mantyla, A. W., Bograd, S. J., & Venrick, E. L. (2008). Patterns and controls of chlorophyll-  
1139 a and primary productivity cycles in the southern california bight. *Journal of Marine*  
1140 *Systems*, *73*(1-2), 48–60.
- 1141 Marchesiello, P., McWilliams, J. C., & Shchepetkin, A. (2001). Open boundary conditions  
1142 for long-term integration of regional oceanic models. *Ocean modelling*, *3*(1-2), 1–20.
- 1143 Marchesiello, P., McWilliams, J. C., & Shchepetkin, A. (2003). Equilibrium structure and  
1144 dynamics of the california current system. *Journal of physical Oceanography*, *33*(4),  
1145 753–783.
- 1146 Maréchal, D. (2004). A soil-based approach to rainfall-runoff modelling in ungauged catch-  
1147 ments for england and wales.
- 1148 Marmorino, G. O., Smith, G. B., Miller, W. D., & Bowles, J. (2010). Detection of a buoy-  
1149 ant coastal wastewater discharge using airborne hyperspectral and infrared imagery.  
1150 *Journal of Applied Remote Sensing*, *4*(1), 043502.
- 1151 Mason, E., Molemaker, J., Shchepetkin, A. F., Colas, F., McWilliams, J. C., & Sangrà, P.  
1152 (2010). Procedures for offline grid nesting in regional ocean models. *Ocean modelling*,  
1153 *35*(1-2), 1–15.
- 1154 McClatchie, S. (2016). *Regional fisheries oceanography of the california current system*.  
1155 Springer.
- 1156 McGillicuddy Jr, D. J. (2016). Mechanisms of physical-biological-biogeochemical interaction  
1157 at the oceanic mesoscale.
- 1158 McLaughlin, K., Dickson, A., Weisberg, S. B., Coale, K., Elrod, V., Hunter, C., ... others  
1159 (2017). An evaluation of isfet sensors for coastal ph monitoring applications. *Regional*  
1160 *Studies in Marine Science*, *12*, 11–18.
- 1161 McLaughlin, K., Meredith, H., Robertson, G., Beck, C., Ho, M., Kessouri, F., ... Weisberg,  
1162 S. (2021). Influence of anthropogenic nutrient inputs on rates of coastal ocean nitrogen  
1163 and carbon cycling in the southern california bight, usa. *Earth and Space Science Open*  
1164 *Archive (ESSOAr)*.
- 1165 McLaughlin, K., Nezlin, N. P., Howard, M. D., Beck, C. D., Kudela, R. M., Mengel, M. J.,  
1166 & Robertson, G. L. (2017). Rapid nitrification of wastewater ammonium near coastal  
1167 ocean outfalls, southern california, usa. *Estuarine, Coastal and Shelf Science*, *186*,  
1168 263–275.
- 1169 McLaughlin, K., Nezlin, N. P., Weisberg, S. B., Dickson, A. G., Booth, J. A. T., Cash,  
1170 C. L., ... others (2018). Seasonal patterns in aragonite saturation state on the  
1171 southern california continental shelf. *Continental Shelf Research*, *167*, 77–86.



- 1172 McWilliams, J. C. (2007). Irreducible imprecision in atmospheric and oceanic simulations.  
 1173 *Proceedings of the National Academy of Sciences*, *104*(21), 8709–8713.
- 1174 McWilliams, J. C. (2016). Submesoscale currents in the ocean. *Proceedings of the Royal*  
 1175 *Society A: Mathematical, Physical and Engineering Sciences*, *472*(2189), 20160117.
- 1176 Middelburg, J. J., Soetaert, K., Herman, P. M., & Heip, C. H. (1996). Denitrification in  
 1177 marine sediments: A model study. *Global Biogeochemical Cycles*, *10*(4), 661–673.
- 1178 Moll, A., & Radach, G. (2003). Review of three-dimensional ecological modelling related to  
 1179 the north sea shelf system: Part 1: models and their results. *Progress in Oceanography*,  
 1180 *57*(2), 175–217.
- 1181 Moore, J. K., Doney, S. C., & Lindsay, K. (2004). Upper ocean ecosystem dynamics and iron  
 1182 cycling in a global three-dimensional model. *Global Biogeochemical Cycles*, *18*(4).
- 1183 Nagai, T., Gruber, N., Frenzel, H., Lachkar, Z., McWilliams, J. C., & Plattner, G.-K.  
 1184 (2015). Dominant role of eddies and filaments in the offshore transport of carbon and  
 1185 nutrients in the California Current System. *Journal of Geophysical Research: Oceans*,  
 1186 *120*(8), 5318–5341.
- 1187 Nash, J., & Sutcliffe, J. (1970). River flow forecasting through conceptual models part i  
 1188 a discussion of principles. *Journal of Hydrology*, *10*(3), 282 - 290. Retrieved from  
 1189 <http://www.sciencedirect.com/science/article/pii/0022169470902556> doi:  
 1190 [https://doi.org/10.1016/0022-1694\(70\)90255-6](https://doi.org/10.1016/0022-1694(70)90255-6)
- 1191 Nezlin, N. P., McLaughlin, K., Booth, J. A. T., Cash, C. L., Diehl, D. W., Davis, K. A.,  
 1192 ... others (2018). Spatial and temporal patterns of chlorophyll concentration in the  
 1193 southern california bight. *Journal of Geophysical Research: Oceans*, *123*(1), 231–245.
- 1194 Nezlin, N. P., Sutula, M. A., Stumpf, R. P., & Sengupta, A. (2012). Phytoplankton  
 1195 blooms detected by seawifs along the central and southern california coast. *Journal*  
 1196 *of Geophysical Research: Oceans*, *117*(C7).
- 1197 Ocean Protection Council. (2018). *State of california ocean acidification action plan*. Re-  
 1198 trieved from <https://www.opc.ca.gov/oa-action-plan/>
- 1199 Regaudie-de Gioux, A., Lasternas, S., Agustí, S., & Duarte, C. M. (2014). Comparing  
 1200 marine primary production estimates through different methods and development of  
 1201 conversion equations. *Frontiers in Marine Science*, *1*, 19.
- 1202 Renault, L., Hall, A., & McWilliams, J. C. (2016a). Orographic shaping of U.S. West Coast  
 1203 Wind Profiles During the Upwelling Season. *Climate Dynamics*, 1–17.
- 1204 Renault, L., Hall, A., & McWilliams, J. C. (2016b). Orographic shaping of us west coast  
 1205 wind profiles during the upwelling season. *Climate Dynamics*, *46*(1-2), 273–289.
- 1206 Renault, L., Masson, S., Arsouze, T., Madec, G., & McWilliams, J. C. (2020). Recipes  
 1207 for how to force oceanic model dynamics. *Journal of Advances in Modeling Earth*  
 1208 *Systems*, *12*(2), e2019MS001715.
- 1209 Renault, L., McWilliams, J. C., Kessouri, F., Jousse, A., Frenzel, H., Chen, R., & Deutsch,  
 1210 C. (2021). Evaluation of high-resolution atmospheric and oceanic simulations of the  
 1211 california current system. *Progress in Oceanography*, *195*, 102564.
- 1212 Renault, L., Molemaker, M. J., Gula, J., Masson, S., & McWilliams, J. C. (2016). Control  
 1213 and stabilization of the gulf stream by oceanic current interaction with the atmosphere.  
 1214 *Journal of Physical Oceanography*, *46*(11), 3439–3453.
- 1215 Renault, L., Molemaker, M. J., McWilliams, J. C., Shchepetkin, A. F., Lemarié, F., Chelton,  
 1216 D., ... Hall, A. (2016). Modulation of wind work by oceanic current interaction with  
 1217 the atmosphere. *Journal of Physical Oceanography*, *46*(6), 1685–1704.
- 1218 Sailley, S., Vogt, M., Doney, S., Aita, M., Bopp, L., Buitenhuis, E., ... Yamanaka, Y.  
 1219 (2013). Comparing food web structures and dynamics across a suite of global marine  
 1220 ecosystem models. *Ecological Modelling*, *261*, 43–57.
- 1221 Savchuk, O. P., & Wulff, F. (2007). Modeling the baltic sea eutrophication in a decision  
 1222 support system. *AMBIO: A Journal of the Human Environment*, *36*(2), 141–148.
- 1223 Seegers, B. N., Birch, J. M., Marin III, R., Scholin, C. A., Caron, D. A., Seubert, E. L.,  
 1224 ... Jones, B. H. (2015). Subsurface seeding of surface harmful algal blooms observed  
 1225 through the integration of autonomous gliders, moored environmental sample proces-  
 1226 sors, and satellite remote sensing in southern c alifornia. *Limnology and Oceanography*,



- 1227 60(3), 754–764.
- 1228 Severmann, S., McManus, J., Berelson, W. M., & Hammond, D. E. (2010). The continental  
1229 shelf benthic iron flux and its isotope composition. *Geochimica et Cosmochimica Acta*,  
1230 74(14), 3984–4004.
- 1231 Shchepetkin, A. F., & McWilliams, J. C. (2005). The regional oceanic modeling system  
1232 (roms): a split-explicit, free-surface, topography-following-coordinate oceanic model.  
1233 *Ocean modelling*, 9(4), 347–404.
- 1234 Shchepetkin, A. F., & McWilliams, J. C. (2009). Correction and commentary for “Ocean  
1235 forecasting in terrain-following coordinates: Formulation and skill assessment of the  
1236 regional ocean modeling system” by Haidvogel et al., *J. Comp. Phys.* 227, pp. 3595–  
1237 3624. *Journal of Computational Physics*, 228(24), 8985–9000.
- 1238 Shchepetkin, A. F., & McWilliams, J. C. (2011). Accurate boussinesq oceanic modeling  
1239 with a practical, stiffened equation of state. *Ocean Modelling*, 38(1-2), 41–70.
- 1240 Skamarock, W. C., & Klemp, J. B. (2008). A time-split nonhydrostatic atmospheric model  
1241 for weather research and forecasting applications. *Journal of Computational Physics*,  
1242 227(7), 3465–3485.
- 1243 Sutton, A., Wanninkhof, R., Sabine, C., Feely, R., Cronin, M., & Weller, R. (2017). Variabil-  
1244 ity and trends in surface seawater pco2 and co2 flux in the pacific ocean. *Geophysical  
1245 Research Letters*, 44(11), 5627–5636.
- 1246 Sutula, M., Ho, M., Sengupta, A., Kessouri, F., McLaughlin, K., McCune, K., & Bianchi,  
1247 D. (2021a, January). *A Baseline of Terrestrial Freshwater and Nitrogen Fluxes to  
1248 the Southern California Bight, USA*. Zenodo. Retrieved from [https://doi.org/  
1249 10.5281/zenodo.4448224](https://doi.org/10.5281/zenodo.4448224) doi: 10.5281/zenodo.4448224
- 1250 Sutula, M., Ho, M., Sengupta, A., Kessouri, F., McLaughlin, K., McCune, K., & Bianchi,  
1251 D. (2021b). Dataset of terrestrial fluxes of freshwater, nutrients, carbon, and iron to  
1252 the southern california bight, u.s.a. *Data in Brief*, 106802. Retrieved from [https://  
1253 www.sciencedirect.com/science/article/pii/S235234092100086X](https://www.sciencedirect.com/science/article/pii/S235234092100086X) doi: [https://  
1254 doi.org/10.1016/j.dib.2021.106802](https://doi.org/10.1016/j.dib.2021.106802)
- 1255 Taylor, B. L., Wade, P. R., De Master, D. P., & Barlow, J. (2000). Incorporating uncertainty  
1256 into management models for marine mammals. *Conservation Biology*, 14(5), 1243–  
1257 1252.
- 1258 Teel, E. N., Liu, X., Seegers, B. N., Ragan, M. A., Haskell, W. Z., Jones, B., & Levine,  
1259 N. M. (2018). Contextualizing time-series data: quantification of short-term regional  
1260 variability in the san pedro channel using high-resolution in situ glider data.
- 1261 Todd, R. E., Rudnick, D. L., Davis, R. E., & Ohman, M. D. (2011). Underwater gliders  
1262 reveal rapid arrival of el niño effects off california’s coast. *Geophysical Research Letters*,  
1263 38(3).
- 1264 Uchiyama, Y., Idica, E. Y., McWilliams, J. C., & Stolzenbach, K. D. (2014). Wastewater  
1265 effluent dispersal in southern california bays. *Continental Shelf Research*, 76, 36–52.
- 1266 Wanninkhof, R. (1992). Relationship between wind speed and gas exchange over the ocean.  
1267 *Journal of Geophysical Research: Oceans*, 97(C5), 7373–7382.
- 1268 Warrick, J. A., DiGiacomo, P. M., Weisberg, S. B., Nezlin, N. P., Mengel, M., Jones, B. H.,  
1269 ... Farnsworth, K. L. (2007). River plume patterns and dynamics within the southern  
1270 california bight. *Continental Shelf Research*, 27(19), 2427–2448.
- 1271 Weisberg, S. B., Bednaršek, N., Feely, R. A., Chan, F., Boehm, A. B., Sutula, M., ...  
1272 Newton, J. A. (2016). Water quality criteria for an acidifying ocean: Challenges and  
1273 opportunities for improvement. *Ocean & Coastal Management*, 126, 31–41.
- 1274 Welch, B. L. (1947, 01). THE GENERALIZATION OF “STUDENT’S” PROBLEM  
1275 WHEN SEVERAL DIFFERENT POPULATION VARIANCES ARE INVOLVED.  
1276 *Biometrika*, 34(1-2), 28-35. Retrieved from [https://doi.org/10.1093/biomet/34.  
1277 .1-2.28](https://doi.org/10.1093/biomet/34.1-2.28) doi: 10.1093/biomet/34.1-2.28
- 1278 Winant, C., Dever, E. P., & Hendershott, M. (2003). Characteristic patterns of shelf circula-  
1279 tion at the boundary between central and southern california. *Journal of Geophysical  
1280 Research: Oceans*, 108(C2).
- 1281 Woodson, C. B., & Litvin, S. Y. (2015). Ocean fronts drive marine fishery production and

1282 biogeochemical cycling. *Proceedings of the National Academy of Sciences*, 112(6),  
1283 1710–1715.  
1284 Zheng, G., & DiGiacomo, P. M. (2017). Uncertainties and applications of satellite-derived  
1285 coastal water quality products. *Progress in oceanography*, 159, 45–72.

Accepted Article